

MECHANICAL TECHNOLOGY INC.  
968 Albany-Shaker Rd.  
Latham, N. Y.

MTI-64TR3

LUBRICATION ANALYSIS IN TURBULENT REGIME  
2nd Quarterly Report  
Contract NAS w-771

by

E.B. Arwas, F.K. Orcutt, J.H.Vohr

January 24, 1964

LUBRICATION ANALYSIS IN TURBULENT REGIME

2nd Quarterly Report

by

E.B. Arwas, F.K. Orcutt, J.H. Vohr

E.B. Arwas *F.K. Orcutt, J.H. Vohr*  
Author(s)  
*Charles H. T. Page*  
Approved by  
*Ben. Sternlicht*  
Approved by

Prepared for

NATIONAL AERONAUTICS AND SPACE ADMINISTRATION

Prepared under

NASA Contract NAS w - 771

Technical Manager  
NASA - Lewis Research Center  
Space Electric Power Office  
Joseph P. Joyce  
Robert T. Wainwright

MECHANICAL TECHNOLOGY INCORPORATED

LATHAM, N.Y.

## TABLE OF CONTENTS

	<u>Page</u>
I. INTRODUCTION -----	1
II. SUMMARY OF WORK IN 2nd QUARTER ----	6
III. WORK ITEMS FOR 3rd QUARTER -----	10
IV. DISCUSSION -----	12
A. Theoretical Study -----	12
B. Dynamic Load Tests -----	14
C. Flow Stability Experiments -----	26
APPENDIX 1: Derivation of Turbulent Lubrication Equation -----	34
APPENDIX 2: Analytical Development of Equivalent Stiffness and Damping Factors -----	45
REFERENCES -----	51
FIGURES	

## I. INTRODUCTION

Process fluid lubrication of space power turbo-machinery is necessary for reliability and efficient design. Where the process fluids are liquid metals, as, for example in Rankine Cycle turbo-machinery for space power, the combined effect of high operating speeds and low kinematic viscosities results in turbulence in the bearing fluid film. Until recently, there had been only limited interest in turbulent bearings, so that design data for this condition lags behind that available for laminar bearing films. In order to minimize expensive trial and error approach to bearing design with turbulent fluid films, sufficient design data has to be generated through theoretical analysis and accurate experiments, to bridge the current gap between laminar and super-laminar bearing operation.

In the design of rotors supported in fluid film bearings, both the steady state and the dynamic properties of the bearings must be determined and later coupled with the rotor characteristics in order to arrive at a satisfactory mechanical design. It is important therefore to determine accurately the fluid film, stiffness and damping coefficients in super-laminar operation, as well as the load capacities and attitude angles of the bearings. It is also important to be able to predict the conditions in the fluid film, i.e. laminar, vortex or turbulent and the transition speeds from one region to the other, as functions of the lubricant properties, bearing eccentricity ratio, L/D and other factors, so that the appropriate data can be used in design calculations. It is the purpose of the current work under NASA Contract NAS-w-771, to:

- (a) determine theoretically and through accurate experiments both the steady state characteristics (load capacity and attitude angle) and the dynamic characteristics (stiffness and damping coefficients) of fundamental journal bearing configurations, over wide ranges of eccentricity ratio and Reynolds number, extending well into turbulent regime.

- (b) determine through accurate, fundamental experiments the regimes of operation (laminar, vortex and turbulent) and the transition speeds from one regime to the other as functions of eccentricity ratio, both with and without an imposed axial pressure gradient.
- (c) define the likely problem areas of rotor-bearing dynamics and of bearing power dissipation associated with liquid metal lubrication of space power turbo-machinery.

The experimental study of the steady state and dynamic characteristics of turbulent bearings are being conducted on a specially designed test rig using a low viscosity (0.65 c.s.) silicone oil. The parallel theoretical analysis and calculations are based on a turbulent lubrication theory that was generated at M.T.I., using the formulations of eddy diffusivity of Reichardt (Ref. 1) and Elrod (Ref.2), as well as the classical test data on turbulent flows in pipes, channels and boundary layers. The fundamental tests on flow stability, transition speeds and friction torque, in the various flow regimes are being made both visually and by torque measurements using a variable speed rotating cylinder test rig and silicone oils of different viscosities (20, 5 and 0.65 c.s.).

The program has three parts as follows:

- A. Theoretical Study
- B. Dynamic Load Tests
- C. Flow Stability Tests

These have the following work items:

A. Theoretical Study

- 1. Refine and program the turbulent flow lubrication theory to include the time dependent terms needed to calculate bearing dynamic properties.

2. Calculate dynamic properties for a range of design and operating parameters and correlate results with experimental measurements.
3. Present data on stiffness and damping of turbulent bearings in non-dimensional form to permit extrapolation to lubricants with different densities and viscosities.
4. From such extrapolation and from consideration of rotor dynamics with flexible shafts, define likely problem areas of rotor-bearings systems for space power.

B. Dynamic Load Tests

1. Design and construct single-test-bearing apparatus incorporating means for applying known dynamic loads of independently controllable frequency to the test bearing and then measuring the response of the bearing.
2. Measure static and dynamic response of bearings operating in the turbulent flow regime. The bearing design parameters, experimental operating parameters and experimentally measured variables are as follows:

Design Parameters (Number of values to be investigated given in parenthesis)	Operating Parameters	Measured Variables
Arc Length, $\beta$ (2)	Reynolds Number	Eccentricity Ratio
Center of Pressure $\theta_p$ , (1)	Steady Load	Attitude Angle
Clearance Ratio, $C/R$ , (1)	Dynamic Load	Stiffness
Slenderness Ratio, $L/D$ , (1)	Frequency	Damping
Supply Pressure $P_s$ (2)		

C. Flow Stability Tests

Conduct fundamental experiments utilizing MTI's Flow Stability Test Rig which consists of a rotating inner and a stationary outer cylinders, similar in concept to the one used by G.I. Taylor to demonstrate vortex flow. These experiments will determine the

manner in which flow structure varies with eccentricity ratio, Reynolds Number and end leakage (L/D effect). They will serve to define the regions of transition to vortex and turbulent flow in bearing films and, hence, the ranges in which laminar and turbulent theories should be applied in bearing design.

The program schedule chart follows. In the subsequent sections of this report, the progress in the second quarter and the work items for the third quarter are listed. Finally, a discussion section is given which describes the work performed during the second quarter in greater detail.

	1	2	3	4	5	6	7	8	9
<b>A. THEORETICAL STUDY</b>									
1.	Analysis & Programming of Turbulent Lubrication Equation, including Dynamic Load Terms & Comparison with Existing Data.								
2.	Calculation of Bearing Performance for Comparison with Dynamic Load Test Data.								
3.	Non-Dimensional Stiffness & Damping Data for Turbulent Bearings.								
4.	Definition of Likely Problem Areas of Rotor-Bearing Design for Space Power Turbo-Machinery.								
<b>B. DYNAMIC LOAD TESTS</b>									
1.	(a)	Design Test Rig.							
	(b)	Manufacture & Install Test Rig							
	(c)	Check Out Test Rig							
2.	(a)	Measurement of Steady State & Dynamic Bearing Performance							
	(b)	Measurement Pressure Profile							
<b>C. FLOW STABILITY TESTS</b>									
1.	Check out Test Rig								
2.	(a)	Measurement of Transition to Vortex Flow							
	(b)	Measurement of Transition to Turbulent Flow							
	(c)	Measurement of Effects of Axial Pressure Gradient on Transition to Vortex & Turbulent Flows.							



## II. SUMMARY OF PROGRESS DURING 2nd QUARTER

### A. Theoretical Study

1. The turbulent lubrication analysis, that was generated at M.T.I. in connection with other work on turbulent lubrication, was extended, under the current study, to include dynamic loading and squeeze film velocities. The bearing equation, including the time dependent terms has been programmed for solution to I.B.M. 7090 computer.
2. A preliminary calculation of the dimensionless stiffness and damping coefficients of plain circular and partial arc bearings, over a range of Reynolds Numbers up to 12,000 was made. Subsequently however, an error in the computer program logic was found which affected some of the calculated data. This program error has been corrected and the calculations were repeated. The data is currently being prepared in the form of design charts.
3. Two auxiliary computer programs were written to facilitate the reduction of the dynamic load test data. The first of these uses the readings of each set of eight data points to compute the corresponding values of the eight spring and damping coefficients, for direct comparison with the theoretical values of these coefficients. The second computer program is based on an analysis (which is given in Appendix 2 of this report) wherein the sets of eight spring and damping coefficients are reduced to sets of four equivalent spring and damping coefficients, which are more convenient for design calculations on rotor-bearing dynamics. (These four equivalent coefficients are similar to the ones used by Hagg and Sankey (Ref.3) in their theoretical and experimental study of dynamic bearing characteristics in laminar regime, except that the orthogonal reference axes used in Ref. 3 are the major and

minor axes of the elliptical orbit of the shaft center, whereas in our study the horizontal and vertical planes are used as reference axes).

## B. Dynamic Load Tests

1. The manufacturing of the test rig and test bearings was completed. The test rig was installed, instrumented and checked out, after which the experimental program was started.
  
2. An initial set of steady state load tests were conducted with the  $360^\circ$  plain circular bearing with an oil inlet feed hole at the top of the bearing. It became quickly apparent however, that due to the low unit loads used in these tests, the load capacity and, to a greater extent, the attitude angles are greatly influenced by the feeding pressures used. At low feed pressures the bearing is oil starved. On the other hand, at low eccentricity ratios and higher feed pressures, the subambient pressures generated in the diverging region result in attitude angles that approach the  $90^\circ$  value predicted by the classical Sommerfeld solution which allows for a continuous, unruptured film. In order to obtain data that is generally valid (rather than restricted to the particular test bearing and test conditions), considerable trial and error would be required to establish appropriate feeding conditions over the range of operating conditions. This was the approach used when this problem was encountered in the tests described in Ref. 4. In the present case, it was decided that such trial and error procedure would not be satisfactory particularly since both steady state and dynamic test data is desired. It was decided therefore not to conduct dynamic load tests with the plain circular bearing, only at eccentricity ratios greater than 0.65, where the

effect of the feeding condition is much reduced and, (b) to conduct the bulk of the test effort in this program, including the pressure profile measurements, with the partial arc bearings, where the feed effects can be eliminated. (It should be noted here that the effect of feeding pressures that were found in tests are also, an important consideration in high speed, liquid metal lubricated bearings. The reason for this is that the mean unit loading of such bearings, due to low viscosity and relatively large clearances are of order  $10^1$  psig, just as in the case of the current test bearing. Subambient pressures as low as -5 psig can be generated in the diverging regions of such high speed bearings, depending on geometry, feeding conditions, vapor pressure and other factors. Thus, the subambient pressures are only moderately smaller in magnitude than the positive pressures generated hydrodynamically in the converging regions of the bearing and correspondingly large attitude angles may be encountered. This has not been the case in prior experience with bearings lubricated with conventional oils, where the mean unit loading is of order  $10^2$ . In these cases, the effect of the subambient pressures in the converging region is generally negligibly small).

3. The steady state load tests were conducted with the 4" diameter, 4" long,  $100^\circ$  partial arc bearing with  $2 \times 10^{-3}$  in/in clearance ratio, over a range of mean clearance Reynolds Numbers from 1665 to 8314. The agreement between experimental and theoretical load capacity was generally very good and provided encouraging verification of the theory. Comparison of measured and calculated attitude angles was also satisfactory, however there was some scatter of test data at low eccentricity ratios, below 0.3, due to the small hydraulic unit loading.

4. The dynamic load tests were started at the end of the current reporting period. These tests and data reduction are currently in progress. A discussion of two methods for evaluating spring and damping coefficients from these tests is given in this report.

C. Flow Stability Tests

1. Transition from laminar to vortex regime was obtained at eccentricity ratios from 0 to 0.891. These were determined both visually and by torque measurements and the data is presented in this report. Comparison with the results other experimental work in this area is also given.
2. Conventional and high speed photographs of the vortex flow of different regions around the circumference of the cylinder, at different eccentricity ratios have been made in order to steady the intensity of vortex action in these regions. The high speed photographs were made with a FASTEX camera on loan from NASA. A motion picture record has also been made of the transition to vortex regime and hence to higher wave instabilities.

### III. WORK ITEMS FOR THIRD QUARTER

#### A. Theoretical Study

1. The calculated steady state and dynamic data will be plotted in dimensionless design charts to show:

Load  
Attitude Angle  
Stiffness Coefficients  
Damping Coefficients

as functions of eccentricity ratio and Reynolds Number for the plain circular and partial arc bearings.

2. The degree of correlation between the theoretical and experimental data will be determined and discussed.

#### B. Dynamic Load Tests

1. Complete the dynamic load tests with the two partial arc bearings and the  $360^\circ$  bearing. The tests with the  $360^\circ$  bearing will be made only at eccentricity ratios greater than 0.65. Load capacity, attitude angle, stiffness and damping coefficients will be obtained as functions of eccentricity ratio up to a Reynolds Number of 16,000 for the  $4 \times 10^{-3}$  in/in clearance ratio bearings and 8000 for the  $2 \times 10^{-3}$  in/in clearance ratio bearing.
2. The measurements of axial and circumferential pressure profiles will be made with a partial arc bearing. Approximately 9 pressure taps will be arranged so as to measure the pressure at 5 points on the circumferential mid plane and at 5 points transversing the bearing axially.

C. Flow Stability Tests

1. Continue the flow stability tests up to a Reynolds Number of approximately 40,000 in order to measure the friction factor as a function of eccentricity ratio and Reynolds Number throughout this range and to determine the flow regimes in this range.
2. Conduct additional tests throughout the range of Reynolds Numbers up to 40,000 and eccentricity ratios up to 0.9, with an axial pressure gradient imposed in the annular region between the cylinders, in order to determine the effects of an axial flow on friction and transition speeds.

#### IV. DISCUSSION

##### A. Theoretical Study

In the first quarterly report (Ref.5) the theoretical analysis of turbulent lubrication that was in progress at M.T.I. was briefly described. This analysis was developed in connection with other work on turbulent lubrication and extended under the current contract to allow treatment of dynamic loads. This analysis has since been completed and is described in References 6 and 7. For convenience of reference, the mathematical analysis leading to the turbulent lubrication equation is reproduced here in Appendix 1.

As noted in Ref. 5 the basis of the analysis is the eddy diffusivity concept, where the shear stress is defined by:

$$\tau = \mu \left( 1 + \frac{\epsilon}{\nu} \right) \frac{du}{dy}^*$$

where the eddy diffusivity is determined from Reichardt's formulation (ref. 1).

$$\frac{\epsilon}{\nu} = k(y^+ - \delta_\ell^+ \tanh \frac{y^+}{\delta_\ell^+})$$

The constants  $k$  and  $\delta_\ell^+$  were obtained by comparison with the published data on turbulent flows in pipes, channels and boundary layers. It was found that these constants are;  $k = 0.4$ , and  $\delta_\ell^+ = 10.7$ . With these values, excellent correlation is found with the experimental data, as shown in Fig. 1 which shows the Universal Velocity Distribution Plot (Ref.8).

The solid line in Fig. 1 is the Three Region Formula curve which satisfies the experimental data throughout the laminar, buffer and turbulent layers, as described in Ref.8. The dashed line in Fig. 1 shows the values calculated by means of the above equations, with  $k = 0.4$  and  $\delta_\ell^+ = 10.7$ . It is seen that very good agreement holds throughout the range. In Appendix 1, the derivation of the turbulent bearing equation is given, starting from the above formulation of the eddy diffusivity for the flow in the fluid film.

---

\* See Nomenclature of Appendix 1 for definition of the symbols.

The resulting equation for turbulent lubrication, given in Appendix 1, was programmed for numerical integration on the I.B.M. 7090. Comparisons have been made with the experimental data Ref. 4. These are shown in Figs. 2a and 2b.

Fig. 2a shows the plots of:

1. the measured values of load vs eccentricity ratio reported in Ref.1, at two super-laminar speeds.
2. the corresponding, theoretical values calculated from the turbulent lubrication equation derived in Appendix 1.
3. the theoretical values calculated using Constantinescu's equation, which was described in our previous quarterly report. (These are shown in Fig. 2a only for the higher speed condition).

This figure shows that there is a good agreement between the turbulent lubrication theory of Appendix 1 and the test data.

Figure 2b shows similar comparisons for attitude angle vs eccentricity ratio. Again agreement is satisfactory.

Further comparison between this theory and test data obtained with a  $60^\circ$  bearing arc at Reynolds Numbers up to 9000 are given in Ref. 7, and show similarly satisfactory correlation. Later in the present report, the steady state data obtained to date in the current program is also compared with theory.

It should be pointed out here that while all the comparisons made to date between steady state experimental data obtained with turbulent bearings and the theoretical predictions using the linearized turbulent bearing equation that was derived at M.T.I. have been encouraging, much work remains to be done in this area. Notably, theoretical work needs to be done to study pressure generation in the vortex regime. Also extensions of the theory are needed to treat cases where the Poiseuille flow components are very large as in the case in turbulent hybrid bearings.



Finally, the computer program that was written to numerically integrate the turbulent bearing equation has been extended to allow also calculations under dynamic load conditions, as required for the current investigation. The stiffness and damping coefficients were computed for the  $360^\circ$  and the  $100^\circ$  bearings, however an error in program logic was subsequently found. This has since been corrected and the values of stiffness and damping coefficients were re-calculated. These are now being plotted in design chart form and used for comparison with the dynamic load test data.

## B. Dynamical Load Tests

### Apparatus and Instrumentation

The dynamic load bearing apparatus, Fig. 3 is described in some detail in Ref. 5. Briefly, the test bearing is located at one end of a long shaft ( $L/D = 10$ ) with preloaded angular contact ball bearings as support bearings at the other end. Steady-state, unidirectional load is applied through a self-aligning ball bearing mounted just outboard of the test bearing. Synchronous rotating load can be applied by unbalance weights secured to a disk on the end of the shaft outboard of the unidirectional load bearing. Rotating load at any frequency independent of shaft rotational speed may be applied by unbalance weights secured to the outer race of a double-row ball bearing whose inner race is mounted on the shaft in place of the disk used for synchronous load. A separate small universal electric motor is coupled to the housing for the outer race of this bearing to drive it and the attached unbalance weights in either direction at any speed up to 20,000 rpm.

The main shaft is coupled to a variable speed (2000 to 11,000 rpm) electric drive by a flexible-disk coupling. Unidirectional load is applied through a cable and pulley by a large, soft (125 lb/in) coil spring with a maximum capacity of about 1200 lbs.

Lubricant is supplied to the test bearing by an air-motor driven gear pump and is scavenged from each end by separate electric motor driven positive action pumps. Inlet lubricant temperature is controlled by a cold water-oil heat exchanger and electric immersion heater in the sump. Bearing temperature is measured by a thermocouple mounted flush with the surface at the trailing edge of the pad. The test lubricant is a silicone fluid of 0.65 c.s. viscosity at 77 F and a viscosity temperature coefficient  $(1 - \frac{\text{viscosity at 210 F}}{\text{viscosity at 100 F}})$  of 0.31. Lubricant viscosity used in determinations of Reynolds and Sommerfeld Numbers is taken as being the viscosity at the temperature midway between the oil inlet and bearing trailing edge measurements.

The principal instrumentation items include eddy-current proximity sensors to determine the shaft position within the bearing clearance, piezoelectric crystal force transducers to measure the dynamic component of the force applied to the bearing through the oil film, and magnetic pickups to mark the times when the rotating load is horizontal and vertical. The displacement probes are located outside the scavenging and seal rings thus avoiding the problems associated with a mixture of air and lubricant in the gap between probe face and reference surface. Provision is made for mounting probes at both ends of the test bearing housing. Simultaneous measurements at both ends have indicated that a linear correction for axial probe offset from the bearing center-line assuming a pivot point at the support bearing end is consistent with the estimated accuracy of about four percent of the bearing clearance.

There has been some difficulty with interactions between the horizontal and vertical force gages; that is, application of a force with a known direction results in a response indicating a force applied at a small angle to the actual direction. There are several explanations for this including elastic deformations of the bearing ring and the housing and the fact that the gages respond to shear as well as normal forces. The force gages are calibrated with the shaft rotating by applying known forces to the shaft through the steady-state load bearing. The force gage response to these calibration loads is linear although there is a 20 degree angle between the indicated and actual directions of force application. Correction for this in dynamic load experiments is made by taking the measurements with the oscilloscope set for X - Y presentation and using the lines of indicated direction for horizontal and vertical force as the reference coordinates in place of the normal X - Y grid. Force gage calibrations have been made at several shaft speeds (2000 and 7000 rpm) over a range of eccentricities, achieved by varying average steady-state load, with no significant differences over the range of load variation expected in dynamic load experiments.

The outputs of both force and displacement sensors have been characterized by a certain amount of high frequency "noise" caused by such factors as inhomogeneity of the shaft material, magnetic fields of the shaft, and noise generated by the rolling contact load and support bearings. These effects are eliminated from the transducer signals by passing through a variable electronic filter set for low pass operation. Below synchronous frequency disturbances in the form of partial frequency whirl also occur over part of the range of operation. These effects can be filtered out by a high pass filter stage and meaningful results can be obtained providing the partial frequency whirl amplitude is not large compared with the synchronous orbit amplitude.

### Steady State Load Capacity Experiments

Measurements of steady-state load capacity of bearings operating in the super-laminar flow regime are being made for correlation with the turbulent flow theory. There are very few data available in the literature for this purpose and accumulation of this information is a natural preliminary step to dynamic load experiments. These experiments have also served to point out several special problems associated with experimental operation of bearings in superlaminar flow.

### Lubricant Feed Effects

The operating conditions of greatest interest in superlaminar flow bearings are characterized by very low unit loads and large film Reynolds numbers. This combination of conditions has been found to raise to prominence certain effects associated with the supply of lubricant to the bearing which are normally of secondary importance.

The first bearing tested was the 360 degree cylindrical bearing with a single feed hole located 180 degrees from the load direction. It immediately became apparent that the shaft center locus for given conditions of load and speed was dependent on lubricant delivery rate. Very low feed rates resulted in typical starved bearing characteristics - i.e., large eccentricity and low attitude angle. If delivery rate was progressively increased, the eccentricity decreased and attitude angle increased in what appeared to be a nearly continuous fashion until a classical Sommerfeld type of behavior with 90 degree attitude angle and no film rupture was approached. At this point, the feed delivery pressures were large enough so that bearing loading from this cause was significant in terms of the external unit load. Several typical examples of the shaft locus measurements and the effects of feed pressure on them are shown in Fig. 4 . Further increases in feed pressure, above those for which data are given in Fig. 4 , resulted in attitude angles approaching 90 degrees for all values of eccentricity.

A major reason for obtaining data on the 360 degree bearing was the fact that it can be considered as a standard or reference bearing. However, in the idealized standard bearing, film rupture occurs within those regions of the film where subambient pressures would otherwise prevail and lubricant is supplied at a rate sufficient to just make up for end leakage in the loaded region. The problem here is that with the high film Reynolds Numbers and low unit loads of the test bearing at low eccentricities, these standard conditions appear to exist for only a narrow range of lubricant feed conditions which is not readily identifiable.

A second problem with the 360 degree bearing is its tendency to exhibit partial frequency whirl when operating under conditions of moderate to low eccentricity. Up to a point it is possible to operate and obtain data even with whirl because the whirl orbit amplitude is comparatively small due to oil film damping. However, as speed is increased or load is reduced the orbit amplitudes grow until it is no longer possible to adequately filter the whirl frequency which is at about half synchronous frequency from the transducer signals. In addition, there can be a considerable cyclic variation in the synchronous load response caused by the variation in the center position of the synchronous orbit due to whirling motion. Thus, whirl restricts the range of steady-state eccentricity ratios over which dynamic load data may be obtained, especially at high speeds, and especially with the 360 degree cylindrical bearing.

Because of these obstacles to effective experimental operation of the 360 degree bearing, attention was shifted to the partial-arc bearings to reconsider use of the full cylindrical bearing. It has since been decided that the unique role of this bearing as a standard and in particular its importance as a configuration for experimental verification of turbulent flow lubrication theory seems to justify working with it within the limitations on range of eccentricity ratios which appear to exist. On the basis of the limited experience to date it seems probable that meaningful data can be obtained for eccentricity ratios from about .65 to .9 or higher.

The first partial-arc bearing configuration tested is illustrated schematically in Fig. 5a. With this bearing, very large attitude angles were obtained, commonly greater than 90 degrees at light loads, and always larger than theoretical predictions. The explanation for this was believed to be lubricant inertia effects at the bearing arc entrance, that is, build-up of a velocity head in the region just ahead of the step at the bearing entrance resulting in hydraulic side loading. Differential pressure measurements were made between this location and the top of the bearing. Pressure differences of about 1.5 psi at 2000 rpm and up to 5 psi at high speeds were measured. To correct this situation, relief or bypass grooves were cut into the sides of the bearing under the bearing arc as shown in Fig. 5b, to equate pressures at entrance and exit. The grooves extend into the bearing from each side to within 1/4 inch of the centerline so the bearing pad is supported by a 1/2 inch thick web along its centerline. This modification has been effective for conditions resulting in eccentricity ratios greater than about .3. At lower eccentricities the unit loads are so small that even with the bypass grooves there is sufficient hydraulic side loading to significantly affect the attitude angles.

#### Load Capacity of the 100° Arc Bearing

Steady-state load capacity data for the 100 degree arc bearing with bypass grooves and L/D of 1 and  $C/R = 2 \times 10^{-3}$  in/in using the 0.65 c.s. silicone lubricant are plotted in Figs. 6 through 9 for comparison with the theoretical predictions of the eddy viscosity turbulent flow bearing theory. It should be pointed out that the theoretical curves given here were obtained before complete check out of the computer program and, therefore, must be considered to be preliminary. The theoretical curve for Reynolds number of zero (laminar flow) is included on each figure for comparison for load carrying capacity. The agreement between experimental and theoretical results is generally very good and represents encouraging verification of this new, improved turbulent flow lubrication theory. The turbulent flow lubrication theory and supporting experimental data indicate an increase in load carrying capacity over

laminar flow performance with the difference increasing with Reynolds number. This is consistent with previous theoretical and experimental results. There is a noteworthy feature of the data for Reynolds' number of 1665 (Fig. 6 ). The abrupt reduction in load capacity between .8 and .85 eccentricity may be an indication that transition from superlaminar to laminar flow has occurred. There is some indication of a similar change beginning to occur at the highest eccentricity data point for Reynolds' number of 3326 (Fig. 7 ). A well defined similar change in load capacity at the apparent flow transition point has been observed in other experiments with partial-arc bearings in the superlaminar flow regime (Ref. 9) Shaft locus data are plotted in Fig.10 for comparison with the theoretical predictions. Here again the agreement is generally good although there is some scatter. The effects of hydraulic side loading at eccentricities below .3 are evident. The theoretical laminar flow shaft locus curve is also plotted in Fig.10 for comparison. Consistent with the higher load capacity, some increase in attitude angles with higher Reynolds numbers for a given eccentricity ratio is indicated.



### Measurement of Dynamic Load Properties

There are several possible combinations of primary experimental measurements which can be made for subsequent reduction to bearing dynamic properties, depending in part on how these dynamic properties are to be defined. Hagg and Sankey (Ref. 3) in their experimental studies of bearing dynamic properties in the laminar flow regime determined "effective" spring and damping coefficients. These effective coefficients lump together both direct and cross coupling effects to describe the bearing properties with four coefficients; one spring and one damping coefficient for both the major and minor axis of the shaft displacement ellipse. Complete specifications of the bearing dynamic properties must include cross coupling coefficients because of course there is a normal component of the shaft response to any applied force increment. Fig.11 is a typical shaft displacement ellipse showing the various forces acting on the shaft to produce this motion. The elliptical shaft center locus pattern is typical of loaded 360 degrees cylindrical bearings and all partial-arc bearings. The exciting load ( $P$ ), applied at some angle ( $\phi$ ) with the line between instantaneous shaft center and the orbit center, results in the generation of oil film elastic and damping forces. The effective coefficients are determined from the overall shaft response to a known exciting force rotating at synchronous speed in the direction of shaft rotation. These effective coefficients are applicable only to dynamic loads applied at synchronous frequency and they are dependent on the dynamical characteristics of the entire rotor-bearing system from which the measurements were obtained. A complete description of bearing dynamic properties applicable to any loading frequency and characteristic of the test bearing alone requires 4 coefficients each for elastic and damping forces to describe direct and cross coupling effects in each of two orthogonal directions. In the following sections, alternate combinations of measurements and approaches to data reduction for the dynamic load bearing apparatus are described.

### Direct Determination of Bearing Stiffness and Damping

From measurements of shaft locus, bearing force, and exciting force magnitude and position, it is possible to determine the bearing dynamic properties directly from summation of the bearing forces as follows:

$$\begin{aligned} K_{xx}x + K_{yy}y + C_{xx}\dot{x} + C_{xy}\dot{y} &= F_x \\ K_{yy}y + K_{yx}x + C_{yy}\dot{y} + C_{yx}\dot{x} &= F_y \end{aligned}$$

where K & C are the fluid film stiffness and damping coefficients respectively. F is the fluid film force and x, y are the orthogonal coordinates, as shown in Fig. 11.

There are a total of eight direct and cross coupling coefficients to be determined so it is necessary to have eight independent points. Two data points (one in the x and one in the y direction) come from each point on the shaft orbit and two independent points of measurement exist for each characteristic orbit so there are just four data points available for any one set of operating conditions. However, by changing the frequency of load application with no change in other conditions, it is possible to obtain a new characteristic shaft locus orbit and obtain four more independent data points. Therefore, direct determination of bearing properties requires two sets of simultaneous measurements of shaft locus and bearing force for each of two frequencies of load rotation.

This is the most direct, preferred means of determining the complete bearing dynamic properties. However, because of some concern over the cross coupling effects noted in the force gaging system and over possible effects of loading frequency on these effects, an alternate approach which can be used to determine bearing dynamic properties without using the bearing force measurements has been developed.

The "effective" dynamic property coefficients of the test bearing can be determined from measurements of dynamic motion of the shaft at two places, the assumption of a rigid shaft and solution of the equation of motion of the rotor-bearing system. The analysis is described in detail in Appendix 2.

Briefly, the system equations of motion are reduced to much more simple equations describing an equivalent system. These equations are of the form:

$$M\ddot{x} + K'_x \dot{x} + C'_x \ddot{x} = \cos\omega t$$

$$M\ddot{y} + K'_y \dot{y} + C'_y \ddot{y} = \sin\omega t$$

where  $M$ ,  $K'$  and  $C'$  are equivalent mass, spring constant and damping coefficient respectively. Two independent sets of values of  $x$ ,  $\dot{x}$ ,  $\ddot{x}$ ,  $y$ ,  $\dot{y}$  and  $\ddot{y}$  are obtained from the measured shaft locus at the test bearing assuming a constant angular velocity of the shaft center about the orbit center. Thus four effective dynamic property coefficients which are dependent on the system dynamics and the load frequency can be obtained from a single set of operating conditions.

Comparison between the eight direct and cross coupling coefficients predicted by the theory and the effective coefficients determined in the above described way can be done by reducing the direct and cross coupling coefficients to effective coefficients as described in Appendix 2. The converse procedure is not possible with one set of effective coefficients since there is no unique solution. However, it should be possible to determine the direct and cross coupling coefficients, which are independent of load frequency or system dynamic characteristics, from two independent sets of effective coefficients obtained from two experiments with different load frequency.

### Dynamic Load - Experimental Measurements

Preliminary dynamic load experiments have been conducted using the 100 degree partial arc bearing,  $C/R = 2 \times 10^{-3}$  in/in to establish procedures and refine the apparatus and instrumentation. Because of their number, the requirement of simultaneous measurement and the necessity for signal filtering, the collection of data is comparatively complex and requires considerable care. The necessary procedures and equipment refinements appear to have been made and the collection of data for analysis and reduction has very recently begun. These data have not yet been reduced to bearing dynamic properties.

The necessary measurements for both of the afore described procedures for bearing dynamic property determination are being made. That is, shaft motion at both test bearing and support bearing, bearing force, and exciting force magnitude, direction and frequency. Comparison of the results obtained from the alternate procedures will be made. If the results compare well, the direct measurement approach will probably be used exclusively for the bulk of the experiments. For each condition of shaft speed and steady-state load, measurements at two dynamic load frequencies will be made to obtain the complete direct and cross coupling dynamic property coefficients.

Simultaneous position and force measurements at two points on the shaft center orbit are obtained by using magnetic pickups to mark the times when the exciting force is in each of two orthogonal positions. The pulses from the magnetic pickups can be superimposed on the force or displacement gage signals to mark the times for measurement. The magnitude of the exciting force is determined from knowledge of the unbalance weight, its distance from the shaft center and its rotational speed. The direction of the exciting force is known from knowledge of the angular position of the magnetic pickups which mark its passage and which signal the points for force and displacement measurement.

### Oil Film Pressure Measurements

Limited low frequency response measurements of oil film pressure are planned for comparison with the predictions of the turbulent flow lubrication theory. Originally it was intended to make these measurements with a 360 degree arc bearing by rotating the direction of applied steady-state load with respect to a single axial row of measurement taps. Because of the problem which has been encountered with variation in performance with lubricant supply conditions for the 360 degree arc bearing it is now considered advisable to make the measurements with a partial arc bearing. The effects of lubricant supply conditions would be aggravated by a change in load direction with respect to the inlet hole. Use of a circumferential groove for feeding to avoid this is not feasible because the available turbulent flow theory computer program does not include provision for an axial pressure gradient from one end of the bearing to the other.

Approximately nine pressure taps arranged in the form of a cross with five across the bearing at the center of the arc and five around the bearing at or near its mid-plane will be used if possible. If access for this many taps is not available, the axial row will extend to one side only.

### C. Flow Stability Experiments

The flow in the clearance gap between a rotating inner cylinder and a stationary outer cylinder develops regularly spaced pairs of toroidal vortices when the rotational speed of the inner cylinder exceeds a certain critical value. The flow pattern in these vortices is shown in Fig.12. The vortex tubes extend completely around the cylinder so that a typical fluid particle travels around the cylinder in a helical path. These vortices are commonly called Taylor vortices after G.I.Taylor who first analytically predicted the critical speed at which they would occur (Ref.10 ). For the case of concentric cylinders, the phenomenon of Taylor vortices has been extensively studied both analytically and experimentally. For non-concentric cylinders however, the problem of the onset of Taylor vortices has not been solved analytically and, moreover, has not been studied experimentally in any detail.\* The prediction of the onset of Taylor vortices in the flow between non-concentric cylinders is of considerable practical importance in connection with journal bearings. Although a Taylor vortex flow, strictly speaking, is still a laminar flow and not a true turbulent flow, the transition to a Taylor vortex flow is effectively similar to the transition to a turbulent flow in that both transitions result in a drastic change in the torque vs speed relations and the velocity profile for the flow. For most journal bearings, the transition to Taylor vortex flow will occur before the transition to turbulence. Therefore, the Taylor vortex transition may be considered to be of greater importance in connection with hydrodynamic bearings than is the transition to true turbulence.

For concentric cylinders in which the ratio of the clearance gap to inner cylinder radius is small, i.e. less than 0.1, the critical speed of the inner cylinder for Taylor vortices to occur is given approximately by

$$\sqrt{1/2 T_a} = \frac{\Omega_1 R_1 d}{\nu} \sqrt{\frac{2d}{R_1 + R_2}} = 41.2$$

---

\* A brief visual study of Taylor vortices in the flow between non-concentric rotating cylinders has been made by J.A.Cole (Ref.11). This work is discussed later along with the results of the present investigation.

where

- $T_a$  = Taylor Number
- $\Omega_1$  = Rotational speed inner cylinder-radians/sec.
- $R_1$  = Radius inner cylinder-in.
- $R_2$  = Radius outer cylinder-in.
- $d$  = Clearance between cylinders-in.
- $\nu$  = Kinematic viscosity of fluid-in<sup>2</sup>/sec.

When the inner cylinder is moved to an eccentric position within the outer cylinder, the increased clearance in the wide region between the cylinders results in a decrease of stability of the flow in this region. On the other hand, the negative pressure flow that occurs in the wide part of the annular clearance between non-concentric cylinders tends to stabilize the flow against the onset of Taylor vortices. A theoretical examination of the stabilizing effect of this negative pressure flow was made by DiPrima (Ref.12). This analysis led to the conclusion that, for small eccentricities, the stability of flow between rotating cylinders should be less than that for concentric cylinders, whereas, at higher eccentricities, it should be greater. DiPrima's analysis, however, considered only the local stability of velocity profiles at each circumferential station and was not an analysis of the stability of the circumferential flow as a whole.

In order to resolve this important question of Taylor vortex instability between non-concentric cylinders, a test rig was built at MTI to study the problem experimentally. A complete description of this test rig was given in the last quarterly progress report. The important dimensions of the test apparatus are:

- Inner cylinder O.D. - 3.64 in
- Outer cylinder I.D. - 4.00 in
- Inner cylinder length - 22.27 in

The onset of Taylor vortices in the flow between the inner and outer cylinders was determined by both torque measurements and by visual observation. The torque measurements provided by far the most accurate and unambiguous means of detecting the onset of vortices. Measurements were made for eccentricity ratios from 0 to 0.891. The eccentricity ratio  $e$

is defined as the ratio of the eccentricity of the inner cylinder to the width of the clearance gap. Maximum possible value for the eccentricity ratio is, of course, 1.0. The fluid used in the test rig was a silicone oil having 20 centistoke kinematic viscosity. Visualization of the flow was accomplished by a suspension of very fine aluminum particles in the silicone oil.

In Fig. 13 is shown a picture of the test rig just at the speed at which Taylor vortices are beginning to develop in the flow (2.69 rev/sec.) The eccentricity ratio for this figure is  $\epsilon = 0.475$ . The photograph is of the wide portion of the annulus. At the conditions shown, the vortices do not remain steady in the flow but shift with time, developing in some places and fading in others. This unsteady vortex activity had no measurable effect on the cylinder torque.

In Fig. 14 is shown the test rig just at the speed where the torque measurements indicate transition to developed Taylor vortex flow (2.99 rev/sec). This is the speed at which the vortices are steadily and fully developed in the flow. One should note that there is about a 10% difference between the speed at which unsteady vortex activity first appears in the flow and the transition speed at which steady vortex flow occurs.

For comparison purposes, Fig. 15 shows fully developed vortices in the test rig for the case where the cylinders are concentric. The axial spacing of the vortices is the same in both the concentric and eccentric cases. In the eccentric case, however, there are no vortices at the ends of the cylinders. This is due to the considerable axial flow that occurs at the ends of the eccentric cylinders which stabilizes the flow near the ends against development of vortices.

In Fig. 16 is shown a close up photograph of the vortex flow near the widest part of the annulus between the cylinders when the eccentricity ratio was 0.475. Direction of rotation of the inner cylinder is from right to left in the photograph. The stream lines of the vortex flow are clearly



indicated by streaks of the fine aluminum powder suspended in the fluid. The directions of the stream lines are shown in the diagram below the photograph.

When the cylinders are concentric, the vortex activity in the flow is symmetrical around the cylinders. When the cylinders are eccentric, however, the intensity of vortex activity varies considerably around the cylinder although the axial wavelength of the vortices remains constant. This circumferential variation in vortex intensity is shown in Fig. 17 where a set of 18 photographs taken at  $20^\circ$  intervals around the test rig are assembled into a single "unwrapped" view of the flow around the cylinders. The eccentricity ratio for this figure is 0.475. The widest part of the annulus between the cylinders is at  $\theta = 0^\circ$  and the narrowest portion is at  $\theta = 180^\circ$ . Rotation of the inner cylinder is in the direction of increasing  $\theta$ . The dark vertical lines at  $\theta = 107^\circ$ ,  $227^\circ$  and  $347^\circ$  in Fig. 17 are the tie rods connecting the upper and lower flanges of the test rig.

As can be seen, the region of strongest vortex activity is in the widest part of the annulus and is centered at approximately  $\theta = 50^\circ$ . Progressively downstream of this, as the annular clearance decreases, the vortex activity damps out until at  $\theta = 180^\circ$  (narrowest part of the annulus) the stream lines appear to be all parallel to the direction of rotation. A close-up high speed motion picture of the flow at  $\theta = 180^\circ$  did reveal, however, that the velocity at this point varies in magnitude periodically with  $Z$  so that there does appear to be some vortex activity still present at this point. Downstream of  $\theta = 180^\circ$  the annulus begins to widen again but vorticity continues to be further damped out and reaches an apparent minimum of strength at  $\theta = 230^\circ$ . From  $\theta = 230^\circ$  onward, vorticity begins to steadily increase again as the widest part of the annulus is approached.

As noted earlier, the point at which established Taylor vortex flow began in the annulus between the two cylinders was determined on the basis of torque measurements. In Fig. 18 is shown a typical torque vs. rotational speed curve for the case where the cylinders are concentric. Up to the rotational speed of 2.16 rev/sec the curve is perfectly linear. At the

rotational speed of 2.16 rev/sec the torque curve changes sharply in slope indicating clearly the onset of established Taylor vortices.

In Figs. 18 through 23 are shown torque vs. speed curves measured at different eccentricity ratios up to and including an eccentricity ratio of  $\epsilon = 0.891$ . In all cases, the curves exhibit the same behavior. Up to a certain critical speed the torque vs. speed curve is a straight line passing through the origin of the graph. At the point of onset of Taylor vortices the torque vs. speed curve changes slope. As eccentricity ratio increases, the change in slope of the torque curve at critical speed becomes steadily less abrupt. Below  $\epsilon = 0.7$  the change in slope is sufficiently sharp so as to make it possible to determine the critical speed easily to a precision of better than 2%.

At the higher eccentricities,  $\epsilon = 0.809$  and  $\epsilon = 0.891$ , the torque curve changes slope only slightly at the critical point and the precision with which the critical point can be determined becomes somewhat less, being about 7%. The measurements of torque and rotational speed in each graph are each accurate to within 1%.

Up to and including the eccentricity ratio  $\epsilon = 0.707$  the critical point on the torque vs. speed curves always corresponds to the point at which steady Taylor vortices were observed to be permanently established in the flow. At the two highest eccentricity ratios for which measurement was made, however ( $\epsilon = 0.809$  and  $\epsilon = 0.891$ ) steady Taylor vortex flow was never attained. Instead, the "vortices" that appeared in the flow were irregularly wavy and erratic as was the flow itself. Qualitatively the flow had the appearance of having large scale turbulence. However, the Reynolds number for the flow based on the maximum clearance and the surface velocity of the inner cylinder was only about 700 so that true turbulence should not have been obtained. The torque vs. speed curves for  $\epsilon = 0.809$  and  $\epsilon = 0.891$  still show a break in slope at some critical speed as do the torque curves for lower eccentricities. Whether this break in slope for the two highest eccentricities can still be interpreted as a transition to Taylor vortex flow, however, is open to question.

turbance travels around the cylinder with the flow at approximately the mean velocity of the flow. When the cylinders were eccentric, this vortex wave instability occurred first at a position about  $20^\circ$  to  $40^\circ$  downstream of the widest part of the annulus between the cylinders. A picture showing this wave instability at an eccentricity of  $\epsilon = 0.475$  is presented in Fig. 25.

The dark circles in Fig. 24 show the critical speed at which the wave instability occurred at eccentricities up to 0.707. These transition points were determined visually since the wave instability had no discernible effect on the torque curves. No wave instability transition was observed for  $\epsilon = 0.809$  or  $\epsilon = 0.891$  since no steady Taylor vortex flow was obtained at these eccentricities.

The wave instability transition points in Fig. 24 are seen to be closely parallel to the Taylor vortex instability curve. The region of steady Taylor vortex flow is the region between the curves formed by the wave instability points and the Taylor vortex points.

A comparison of the present experimental data with measurements made earlier by J.A.Cole is shown in Fig. 26. Since Cole's determination was done visually, we have included in Fig. 26 the points at which vortex activity was first observed in our present experiments. Although Cole's data shows considerable scatter his points lie generally below those measured at M.T.I. The nominal radial dimensions of Cole's test rig were

$$R_1 = 1.5 \text{ in.}$$

$$R_2 = 0.6 \text{ in.}$$

The next aspects of Taylor vortex flow between a stationary outer cylinder and an eccentric inner cylinder to be studied with the M.T.I. test rig are: (1) the nature of the flow as Reynolds is increased up to and well beyond the point of true turbulence and (2) the effect of axial flow on Taylor vortices for non-concentric cylinders. The first of these studies, namely

turbance travels around the cylinder with the flow at approximately the mean velocity of the flow. When the cylinders were eccentric, this vortex wave instability occurred first at a position about  $20^\circ$  to  $40^\circ$  downstream of the widest part of the annulus between the cylinders. A picture showing this wave instability at an eccentricity of  $\epsilon = 0.475$  is presented in Fig. 25.

The dark circles in Fig. 24 show the critical speed at which the wave instability occurred at eccentricities up to 0.707. These transition points were determined visually since the wave instability had no discernible effect on the torque curves. No wave instability transition was observed for  $\epsilon = 0.809$  or  $\epsilon = 0.891$  since no steady Taylor vortex flow was obtained at these eccentricities.

The wave instability transition points in Fig. 24 are seen to be closely parallel to the Taylor vortex instability curve. The region of steady Taylor vortex flow is the region between the curves formed by the wave instability points and the Taylor vortex points.

A comparison of the present experimental data with measurements made earlier by J.A.Cole is shown in Fig. 26. Since Cole's determination was done visually, we have included in Fig. 26 the points at which vortex activity was first observed in our present experiments. Although Cole's data shows considerable scatter his points lie generally below those measured at M.T.I. The nominal radial dimensions of Cole's test rig were

$$R_1 = 1.5 \text{ in.}$$

$$R_2 = 0.6 \text{ in.}$$

The next aspects of Taylor vortex flow between a stationary outer cylinder and an eccentric inner cylinder to be studied with the M.T.I. test rig are: (1) the nature of the flow as Reynolds is increased up to and well beyond the point of true turbulence and (2) the effect of axial flow on Taylor vortices for non-concentric cylinders. The first of these studies, namely

the high Reynolds Number runs, will involve both torque measurements as well as visual observations of the flow. High speed motion pictures of the flow will also be taken. It is expected that these high speed runs will be made at nominal eccentricities of 0, 0.4 and 0.8. Reynolds Numbers up to 40,000 will be attained.

The axial flow runs will involve visual observation of the flow only. These runs will also be made at the nominal eccentricities of  $\epsilon = 0$ , 0.4 and 0.8

APPENDIX 1

DERIVATION OF THE LINEARIZED  
TURBULENT LUBRICATION EQUATION

by

C. H. T. Pan

C. Ng

1. NOMENCLATURE FOR APPENDIX 1

$B_x, B_z$	$\frac{h^2}{\mu V} \frac{\partial p}{\partial x}, \frac{h^2}{\mu V} \frac{\partial p}{\partial z}$
C	mean bearing clearance
$C_f$	coefficient of wall friction in the Couette flow
D	journal diameter
$f_c(\eta), g_c(\eta)$	functions of $\eta$ containing the parameter $h_c^+$
$g(y^+)$	a function giving the universal velocity profile in turbulent shear flows
$G_x$	coefficient which depends on $R_h$ ; defined by equation (36)
$G_z$	coefficient which depends on $R_h$ ; defined by equation (37)
$h_c^+$	$\frac{h}{\nu} \sqrt{\frac{\tau_c}{\rho}}$
h	local bearing gap
$H_x$	$hG_x^{1/3}$
$H_z$	$hG_z^{1/3}$
k	mixing length constant, taken to be 0.4 in the present work.
$\ell$	mixing length
L	bearing length
N	rotor speed in revolutions per second.
p	fluid film pressure
$p_a$	ambient pressure
$p_v$	vapor pressure of the fluid
R	journal radius
$R_e$	$VC/\nu$ , mean Reynolds number
$R_h$	$Vh/\nu$ , local Reynolds number
t	time
u	mean circumferential velocity component
$u'$	the fluctuating part of the circumferential velocity component in a turbulent flow

$u^+$	$u/u_\tau$ , dimensionless circumferential velocity
$u_\tau$	$\sqrt{\frac{\tau}{\rho}}$ , velocity parameter
$v'$	the fluctuating part of the transverse velocity component in a turbulent flow
$V$	journal surface speed
$\overline{u'v'}, \overline{w'v'}$	long period time average of $(u'v', w'v')$
$w$	mean axial velocity component
$w'$	the fluctuating part of the axial velocity component in a turbulent flow
$W$	bearing load
$w, z$	circumferential and axial coordinates
$y$	coordinate normal to bearing surface
$y^+$	the dimensionless coordinate for plotting the universal velocity profile, $u_\tau y/\nu$
$y'$	dummy variable for $y$
$y_m$	location where $\epsilon/\nu$ is matched
$\delta( )$	variation of $( )$ from that in the Couette flow
$\delta_\ell^+$	a constant related to the thickness of the laminar sublayer, taken to be 10.7 in the present work
$\epsilon$	eddy diffusivity
$\eta$	$y/h$ , dimensionless coordinate normal to the bearing surface
$\eta'$	dummy variable for $\eta$
$\mu$	fluid viscosity
$\nu$	kinematic viscosity
$\omega$	rotor speed in radians per second.
$\theta_p$	angle between entrance edge of the bearing to the line of force
$ \tau $	magnitude of the local shear stress
$\tau_\ell, \tau_u$	lower and upper wall shears
$\tau_w$	shear stress at wall
$\tau_c$	shear stress in the Couette flow
$\tau_{xy}, \tau_{zy}$	shear stress components
$\rho$	mass density of the fluid



## 2. THE GENERALIZED LAW OF WALL

Consider a turbulent shear flow which is steady and two-dimensional on the average, and which is experiencing a shearing stress  $\tau_w$  on the impermeable stationary wall at  $y = 0$ . Under this condition, a large amount of experimental data have shown that the mean velocity profile in a region near the wall can be described by a universal correlation known as the "law of wall".

$$u^+ = g(y^+) \quad (1)$$

where  $u^+ = u/u_\tau$ ,  $y^+ = u_\tau y/\nu$ ,  $u_\tau = (\tau_w/\rho)^{1/2}$

This universal correlation can be used to define an eddy viscosity

$$-\overline{u'v'} = \epsilon \frac{du}{dy} \quad (2)$$

Reichardt<sup>(7)</sup> proposed an empirical formula for  $\epsilon$ ,

$$\frac{\epsilon}{\nu} = k \left[ y^+ - \delta_\ell^+ \tanh \left( \frac{y^+}{\delta_\ell^+} \right) \right] \quad (3)$$

which, according to Ng<sup>(6)</sup>, if the constants  $k$  and  $\delta_\ell^+$  are chosen to be 0.4 and 10.7 respectively, correlates well with all pertinent data.

More recently, it has been demonstrated that the "law of wall" also applies to turbulent shear flows in which the shear stress varies with the transverse coordinate, provided the local shear, instead of the wall shear, is used to define  $u_\tau$ . This conclusion is consistent with the data published by Stratford and Townsend<sup>(14)</sup> on turbulent boundary layers in the presence of an adverse pressure gradient. If we assume isotropy in the turbulent momentum transport process, this generalized "law of wall" can be applied to non-planar mean flows.

In applying equation (3) to channel flows,  $0 \leq y \leq h$ ,  $y^+$  should be re-defined at  $(h-y) u_\tau/\nu$  in the range  $\frac{h}{2} \leq y \leq h$ . This method of separating the effects of the two walls would introduce an abrupt change in the transverse derivative of  $f(y^+)$ . This slight anomaly will be accepted for simplicity.

In summary, the essential features of the generalized "law of wall" are:

1. Reichardt's formula for eddy diffusivity

$$\frac{\epsilon}{\nu} = k \left[ y^+ - \delta_\ell^+ \tanh \left( \frac{y^+}{\delta_\ell^+} \right) \right] \quad (3)$$

is adopted with the numerical constants

$k = 0.4$ , and

$\delta_l^+ = 10.7$ .

2. The velocity parameter,  $u_\tau$ , is based on the magnitude of the total local shear:

$$u_\tau = \sqrt{\frac{|\tau|}{\rho}} \quad (4)$$

3. Each half channel has its own wall.

$$y^+ = \begin{cases} \eta \frac{h}{v} \sqrt{\frac{|\tau|}{\rho}} \\ (1 - \eta) \frac{h}{v} \sqrt{\frac{|\tau|}{\rho}} \end{cases} \quad \text{for} \quad \begin{cases} 0 \leq \eta = \frac{y}{h} \leq \frac{1}{2} \\ \frac{1}{2} \leq \eta \leq 1. \end{cases} \quad (5)$$

### 3. DERIVATION OF THE LINEARIZED TURBULENT LUBRICATION EQUATION

Two additional assumptions will be made in the course of deriving the governing equation for the pressure of the turbulent lubricating film. The first assumption neglects the terms corresponding to mean inertia and variations of shear stresses along the surface coordinates.

$$\frac{\partial \tau_{xy}}{\partial y} = \frac{\partial p}{\partial x} \quad (6)$$

$$\frac{\partial \tau_{zy}}{\partial y} = \frac{\partial p}{\partial z} \quad (7)$$

These equations can be integrated, and taking advantage of the definition of eddy viscosity

$$\tau_{xy}(y) = \tau_{xy}\left(\frac{h}{2}\right) + \left(y - \frac{h}{2}\right) \frac{\partial p}{\partial x} = \mu \left(1 + \frac{\epsilon}{\nu}\right) \frac{\partial u}{\partial y} \quad (8)$$

$$\tau_{zy}(y) = \tau_{zy}\left(\frac{h}{2}\right) + \left(y - \frac{h}{2}\right) \frac{\partial p}{\partial z} = \mu \left(1 + \frac{\epsilon}{\nu}\right) \frac{\partial w}{\partial y} \quad (9)$$

Further integration of equations (3) and (4) yields

$$u(y) = \frac{1}{\mu} \left[ \tau_{xy}\left(\frac{h}{2}\right) \int_0^y \frac{dy'}{1 + \frac{\epsilon}{\nu}} + \frac{\partial p}{\partial x} \int_0^y \frac{\left(y' - \frac{h}{2}\right) dy'}{1 + \frac{\epsilon}{\nu}} \right] \quad (10)$$

$$w(y) = \frac{1}{\mu} \left[ \tau_{zy}\left(\frac{h}{2}\right) \int_0^y \frac{dy'}{1 + \frac{\epsilon}{\nu}} + \frac{\partial p}{\partial z} \int_0^y \frac{\left(y' - \frac{h}{2}\right) dy'}{1 + \frac{\epsilon}{\nu}} \right] \quad (11)$$

In equations (8) through (11),  $\tau_{xy}\left(\frac{h}{2}\right)$  are integration constants which are to be determined by requiring

$$u(h) = V \quad (12)$$

$$w(h) = 0 \quad (13)$$

To simplify the computation of eqs. (3) through (8) a second assumption will now be made—the flow field is a small perturbation of the turbulent Couette flow. That is

$$\tau_{xy} = \tau_c + \delta \tau_x \quad (14)$$

$$\tau_{zy} = \delta \tau_z \quad (15)$$

Now

$$\begin{aligned} |\tau| &= \sqrt{(\tau_{xy})^2 + (\tau_{zy})^2} \\ &= \tau_c + \delta\tau_x + O(\delta^2) \end{aligned} \quad (16)$$

The eddy viscosity, eq. (3), can likewise be approximated by making a small perturbation on the turbulent Couette flow:

$$\begin{aligned} \frac{\epsilon}{\nu}(\eta, |\tau|) &= \frac{\epsilon}{\nu}(\eta, \tau_c) + \delta\tau_x \left. \frac{\partial(\frac{\epsilon}{\nu})}{\partial|\tau|} \right|_{\tau=\tau_c} + O(\delta^2) \\ &= f_c(\eta) - 1 + \frac{\delta\tau_x}{\tau_c} g_c(\eta) + O(\delta^2) \end{aligned} \quad (17)$$

where

$$f_c(\eta) - 1 = k \left[ \eta h_c^+ - \delta_l^+ \tanh\left(\eta \frac{h_c^+}{\delta_l^+}\right) \right] \quad (18)$$

$$g_c(\eta) = \frac{k}{2} \eta h_c^+ \tanh^2\left(\eta \frac{h_c^+}{\delta_l^+}\right) \quad (19)$$

with  $h_c^+ = \frac{h}{\nu} \sqrt{\frac{\tau_c}{\rho}}$

Again, in the righthand sides of equations (18) and (19),  $\eta$  should be replaced by  $(1 - \eta)$  in the range  $\frac{1}{2} \leq \eta \leq 1$ . Thus both  $f_c(\eta)$  and  $g_c(\eta)$  are symmetrical with respect to  $\eta = \frac{1}{2}$ .

### 1. Couette Flow

Before continuing the derivation, we shall first examine the salient features of the turbulent Couette flow. Equation (10) is reduced to

$$u_c(\eta) = \frac{h\tau_c}{\mu} \int_0^\eta \frac{d\eta'}{f_c(\eta')} \quad (20)$$

and

$$u_c(1) = v = \frac{h\tau_c}{\mu} \int_0^1 \frac{d\eta}{f_c(\eta)} \quad (21)$$

Or, in the dimensionless form,

$$R_h = \frac{Vh}{\nu} = (h_c^+)^2 \int_0^1 \frac{d\eta}{f_c(\eta)} \quad (22)$$

which in essence defines the Couette Reynolds' number in terms of the parameter  $h_c^+$ . The last expression can be further rewritten to yield the coefficient of wall friction

$$\begin{aligned} C_f &= \frac{\tau_c}{\frac{1}{2} \rho \left(\frac{V}{2}\right)^2} \\ &= \frac{8 \tau_c}{\rho V^2} \\ &= \frac{8}{R_h \int_0^1 \frac{d\eta}{f_c(\eta)}} \end{aligned} \quad (23a)$$

$$= \frac{8}{h_c^+ \left[ \int_0^1 \frac{d\eta}{f_c(\eta)} \right]^2} \quad (23b)$$

Clearly, this does not explicitly express the commonly accepted power law,  $C_f \sim R_h^{-0.25}$

The above results are identical to those previously given in Ref. 6

## 2. Linearized Pressure-Flow Relations

Substitute eqs. (17) through (19) into eqs. (10) and (11) leaving out terms  $\sim O(\delta^2)$ , and rewrite in terms of the dimensionless coordinates  $\eta$ :

$$\begin{aligned} u(\eta) &= \frac{h\tau_c}{\mu} \int_0^\eta \frac{d\eta'}{f_c(\eta')} + \left(\frac{h}{\mu}\right) \left[ \tau_{xy}(1/2) - \tau_c \right] \int_0^\eta \frac{1}{f_c(\eta')} \left[ 1 - \frac{g_c(\eta')}{f_c(\eta')} \right] d\eta' \\ &\quad - \frac{h^2}{\mu} \frac{\partial p}{\partial x} \int_0^\eta \frac{(\frac{1}{2} - \eta')}{f_c(\eta')} \left[ 1 - \frac{g_c(\eta')}{f_c(\eta')} \right] d\eta' \end{aligned} \quad (24)$$

$w(\eta)$

$$= \frac{h\tau_{zy}(1/2)}{\mu} \int_0^{\eta} \frac{d\eta'}{f_c(\eta')} - \frac{h^2}{\mu} \frac{\partial p}{\partial z} \int_0^{\eta} \frac{(\frac{1}{2} - \eta')}{f_c(\eta')} d\eta' . \quad (25)$$

Now, impose the conditions given by eqs. (12) and (13) and make use of eq. (21) we find

$$0 = \left(\frac{h}{\mu}\right) \left[ \tau_{xy} \left(\frac{1}{2}\right) - \tau_c \right] \int_0^1 \frac{1}{f_c(\eta)} \left[ 1 - \frac{g_c(\eta)}{f_c(\eta)} \right] d\eta \\ - \frac{h^2}{\mu} \frac{\partial p}{\partial x} \int_0^1 \frac{(\frac{1}{2} - \eta)}{f_c(\eta)} \left[ 1 - \frac{g_c(\eta)}{f_c(\eta)} \right] d\eta \quad (26)$$

and

$$0 = \frac{h\tau_{zy}(\frac{1}{2})}{\mu} \int_0^1 \frac{d\eta}{f_c(\eta)} - \frac{h^2}{\mu} \frac{\partial p}{\partial z} \int_0^1 \frac{(\frac{1}{2} - \eta)}{f_c(\eta)} d\eta . \quad (27)$$

Now, since  $f_c(\eta)$  and  $g_c(\eta)$  are symmetrical while  $(\frac{1}{2} - \eta)$  is antisymmetrical about  $\eta = \frac{1}{2}$ , we conclude

$$\int_0^1 \frac{1}{f_c(\eta)} \left[ 1 - \frac{g_c(\eta)}{f_c(\eta)} \right] d\eta \neq 0 \\ \int_0^1 \frac{d\eta}{f_c(\eta)} \neq 0 \quad (28)$$

$$\int_0^1 \frac{(\frac{1}{2} - \eta)}{f_c(\eta)} \left[ 1 - \frac{g_c(\eta)}{f_c(\eta)} \right] d\eta = \int_0^1 \frac{(\frac{1}{2} - \eta)}{f_c(\eta)} d\eta = 0 .$$

Therefore, comparing equations (26), (27) and (28) it is found

$$\tau_{xy}(\frac{1}{2}) = \tau_c \quad (29)$$

and

$$\tau_{zy}(\frac{1}{2}) = 0 \quad (30)$$

Thus equations (24) and (25) can be simplified to

$$\frac{u}{V} = \frac{h\tau_c}{\mu V} \int_0^{\eta} \frac{d\eta'}{f_c(\eta')} - B_x \int_0^{\eta} \frac{(\frac{1}{2} - \eta')}{f_c(\eta')} \left[ 1 - \frac{g_c(\eta')}{f_c(\eta')} \right] d\eta' \\ = \frac{1}{2} + \frac{(h_c^+)^2}{R_h} \int_{\frac{1}{2}}^{\eta} \frac{d\eta'}{f_c(\eta')} - B_x \int_0^{\eta} \frac{(\frac{1}{2} - \eta')}{f_c(\eta')} \left[ 1 - \frac{g_c(\eta')}{f_c(\eta')} \right] d\eta' \quad (31)$$

$$\frac{w}{V} = -B_z \int_0^{\eta} \frac{(\frac{1}{2} - \eta')}{f_c(\eta')} d\eta' \quad (32)$$

where

$$B_x = \frac{h^2}{\mu V} \frac{\partial p}{\partial x}; \text{ and } B_z = \frac{h^2}{\mu V} \frac{\partial p}{\partial z} \quad (33)$$

The corresponding fluxes are

$$\int_0^h u dy = Vh \left( \frac{1}{2} - G_x B_x \right) \quad (34)$$

$$\int_0^h w dy = -Vh G_z B_z \quad (35)$$

where

$$G_x = \int_0^1 d\eta \int_0^{\eta} \frac{(\frac{1}{2} - \eta')}{f_c(\eta')} d\eta' - \frac{g_c(\eta')}{f_c(\eta')} d\eta' \quad (36)$$

$$G_z = \int_0^1 d\eta \int_0^{\eta} \frac{(\frac{1}{2} - \eta')}{f_c(\eta')} d\eta' \quad (37)$$

Note that both  $G_x$  and  $G_z$  depend on  $R_h$  and, therefore, are functions of the local film thickness  $h$ . They have been calculated for  $R_h$  up to  $2.5 \times 10^5$ .

Equations (32), (35), and (37) are, in form, identical to those derived for the plane Poiseuille Flow in Ref. 6. There is a difference, however, in the physical interpretation of  $f_c(\eta)$ . Here  $f_c(\eta)$  gives the eddy diffusivity caused by the Couette shear; whereas the corresponding function for the plane Poiseuille flow in Ref. 6 is caused by the wall shear of the Poiseuille flow.

### 3. Linearized Turbulent Lubrication Equation

The continuity condition for an incompressible fluid film is

$$\frac{\partial}{\partial x} \left( \int_0^h u dy \right) + \frac{\partial}{\partial z} \left( \int_0^h w dy \right) + \frac{\partial h}{\partial t} = 0. \quad (38)$$

Substitute eqs. (33) through (35) into eq. (38) and rearrange,

$$\frac{\partial}{\partial x} \left( \frac{h^3}{\mu} G_x \frac{\partial p}{\partial x} \right) + \frac{\partial}{\partial z} \left( \frac{h^3}{\mu} G_z \frac{\partial p}{\partial z} \right) = \left( \frac{V}{2} \frac{\partial}{\partial x} + \frac{\partial}{\partial t} \right) h. \quad (39)$$

If we define

$$H_x = h G_x^{1/3} \quad \text{and} \quad H_z = h G_z^{1/3} \quad (40)$$

then eq. (39) becomes

$$\frac{\partial}{\partial x} \left( \frac{H_x^3}{\mu} \frac{\partial p}{\partial x} \right) + \frac{\partial}{\partial z} \left( \frac{H_z^3}{\mu} \frac{\partial p}{\partial z} \right) = \left( \frac{V}{2} \frac{\partial}{\partial x} + \frac{\partial}{\partial t} \right) h \quad (41)$$

Equation (41) is, in form, same as the laminar lubrication equation. The effect of turbulence is seen to be equivalent to modifying the effective film thickness by different amounts dependent on the local Reynolds number in the two directions on the left hand side of the equation.

The boundary conditions for the ends are

$$p(x, z = \pm L/2) = p_a \quad (42)$$

The x-wise boundary condition depend on the bearing geometry; for in the case of a full journal bearing,

$$p(x + 2\pi R, z) = p(x, z) \quad (43)$$

The possibility of fluid film rupture is further given by the idealized striation condition

$$p \geq p_v \quad (44)$$

and

$$\frac{\partial p}{\partial x} = 0 \quad \text{when} \quad p = p_v \quad (45)$$

where  $p_v$  is the vapor pressure of the lubricant; presumably it is the minimum pressure that can be sustained by the fluid film.



APPENDIX 2

ANALYTICAL DEVELOPMENT OF EQUIVALENT  
STIFFNESS AND DAMPING FORCES

by

H. Cheng

Analytical Development of Equivalent Stiffness and Damping Factors.

The bearing forces, inertia forces and the external exciting force acting on the experimental rotor are shown in Fig. 27. The meaning of the symbols shown in Fig. 27 are listed as follows:

$O'$	-	center of the guide bearing
$C$	-	center of mass of the rotor
$A$	-	center of the test bearing
$B$	-	point of application of the exciting force
$l_c$	-	distance $O'C$ in.
$l_a$	-	distance $O'A$ in.
$l_b$	-	distance $O'B$ in.
$M$	-	mass of rotor lb.sec <sup>2</sup> /in.
$x'_O, x'_A, x'_C$	-	x coordinates of $O', A, C$ respectively, in.
$y'_O, y'_A, y'_C$	-	y coordinates of $O', A, C$ respectively, in.
$F_y, F_x$	-	bearing forces at $A$
$M_b$	-	mass of the exciting mass (cap screw)
$R$	-	distance of $m_b$ from $B$
$\omega$	-	exciting frequency
$\Omega$	-	angular speed of the shaft
$T_x$	-	x component of the inertia torque
$T_y$	-	y component of the inertia torque
$k_x$	-	radius of gyration about an axis passing through $c$ and parallel to $O'x$
$k_y$	-	radius of gyration about an axis passing through $c$ and parallel to $O'y$
$k_z$	-	radius of gyration about $O'Z$
$\dot{x}$	-	$\frac{dx}{dt}$

Taking moment of all forces about  $O'$ , we have

$$(A1) \quad M \ddot{y}_c - F_y \ell_a + T_x = \ell_b m_b R \omega^2 \sin \omega t$$

$$(A2) \quad M \ddot{x}_c - F_x \ell_a - T_y = \ell_b m_b R \omega^2 \cos \omega t$$

where the bearing forces,  $F_x$  and  $F_y$ , and the inertia torques,  $T_x$  and  $T_y$  are represented by the following expressions,

$$(A3) \quad F_x = -(K_{xx} \dot{x}_a + C_{xx} \ddot{x}_a + K_{xy} \dot{y}_a + C_{xy} \ddot{y}_a)$$

$$(A4) \quad F_y = -(K_{yx} \dot{x}_a + C_{yx} \ddot{x}_a + K_{yy} \dot{y}_a + C_{yy} \ddot{y}_a)$$

$$(A5) \quad T_x = M k_x^2 \left( \frac{\ddot{y}_a - \ddot{y}'_o}{\ell_a} \right) + M (k_y^2 - k_z^2) \Omega \left( \frac{\dot{x}_a - \dot{x}'_o}{\ell_a} \right)$$

$$(A6) \quad T_y = -M k_y^2 \left( \frac{\ddot{x}_a - \ddot{x}'_o}{\ell_a} \right) - M (k_z^2 - k_x^2) \Omega \left( \frac{\dot{y}_a - \dot{y}'_o}{\ell_a} \right)$$

Assuming the shaft is a rigid body, the following geometrical relations prevails,

$$(A7) \quad x_c = x'_o + \left( \frac{\ell_c}{\ell_a} \right) (x_a - x'_o)$$

$$(A8) \quad y_c = y'_o + \left( \frac{\ell_c}{\ell_a} \right) (y_a - y'_o)$$

Substituting (A3) through (A8) into (A1) and (A2) and dividing then by  $\ell_a$ , we have,

$$(A9) \quad M_e \ddot{\bar{x}}_a + \rho \ddot{\bar{x}}'_o + (\bar{K}_{xx} \bar{x}_a + \bar{C}_{xx} \dot{\bar{x}}_a + \bar{K}_{xy} \bar{y}_a + \bar{C}_{xy} \dot{\bar{y}}_a) + \beta (\dot{\bar{y}}_a - \dot{\bar{y}}'_o) = \cos \omega t$$

$$(A10) \quad M_e \ddot{\bar{y}}_a + \rho \ddot{\bar{y}}'_o + (\bar{K}_{yx} \bar{x}_a + \bar{C}_{yx} \dot{\bar{x}}_a + \bar{K}_{yy} \bar{y}_a + \bar{C}_{yy} \dot{\bar{y}}_a) - \beta (\dot{\bar{x}}_a - \dot{\bar{x}}'_o) = \sin \omega t$$

where

$$\begin{aligned}
 M_e &= \frac{M_c}{m_b R L_b} \left[ L_c^2 + \left( \frac{k_x}{\ell_a} \right)^2 \right] \\
 k_x &= k_y \\
 \rho &= \frac{M_c}{m_b R L_b} \left[ L_c (1 - L_c) - \left( \frac{k_x}{\ell_a} \right)^2 \right] \\
 (A11) \quad \beta &= \frac{M_c}{m_b R \omega L_b} \frac{(k_z^2 - k_y^2)}{\ell_a^2} \Omega \\
 \bar{K}_{xx} &= \frac{K_{xx} C}{m_b R \omega^2 L_b} \\
 \bar{C}_{xx} &= \frac{C_{xx} C}{m_b R \omega L_b} \quad \text{etc.} \\
 \bar{x}_a &= x_a / C \quad \text{etc.} \\
 \bar{y}_a &= y_a / C \quad \text{etc.}
 \end{aligned}$$

$C$  = radial clearance of the bearing  
 and  $\dot{x}$  now stands for  $\frac{dx}{d(\omega t)}$ .

For small oscillations of the rotor, the following substitutions can be made,

$$\begin{aligned}
 \bar{x}_a &= A e^{i\omega t} \\
 \bar{y}_a &= B e^{i\omega t} \\
 (A12) \quad \bar{x}'_o &= E e^{i\omega t} \\
 \bar{y}'_o &= F e^{i\omega t}
 \end{aligned}$$

where A, B, E and F are complex amplitudes of oscillation at A and O'.

Substituting (A12) into (A9) and (A10), we have

$$(A13) \quad (\bar{K}_{xx} - M_e + i \bar{C}_{xx}) A + [\bar{K}_{xy} + i (\bar{C}_{xy} + \beta)] B = 1 + \rho E + i \beta F$$

$$(A14) \quad [\bar{K}_{yx} + i (\bar{C}_{yx} - \beta)] A + (\bar{K}_{yy} - M_e + i \bar{C}_{yy}) B = \rho F - i(1 + \beta E)$$

If the motion at  $O'$  is given, then  $E$  and  $F$  become known and Equations (A13) and (A14) can be solved for  $A$  and  $B$  to give

$$(A15) \quad A = \frac{us - vq}{ps - rq}$$

$$(A16) \quad B = \frac{pv - ur}{ps - rq}$$

where

$$(A17) \quad \begin{aligned} p &= \bar{K}_{xx} - M_e + i \bar{C}_{xx} \\ q &= \bar{K}_{xy} + i (\bar{C}_{xy} + \beta) \\ r &= \bar{K}_{yx} + i (\bar{C}_{yx} - \beta) \\ s &= \bar{K}_{yy} - M_e + i \bar{C}_{yy} \\ u &= 1 + \rho E + i\beta F \\ v &= \rho F - i(1 + \beta E) \end{aligned}$$

The dynamic system represented by Eq. (A13) and (A14) can now be reduced to a much simpler equivalent system containing only effective direct stiffness  $K_x'$ ,  $K_y'$  and effective direct damping factors  $C_x'$ ,  $C_y'$  without the cross coupling stiffness and damping factors.

The equations governing the motion of the equivalent system are

$$(A18) \quad M_e \ddot{x}_a + K_x' x_a + C_x' \dot{x}_a = \cos \omega t$$

$$(A19) \quad M_e \ddot{y}_a + K_y' y_a + C_y' \dot{y}_a = \sin \omega t$$

Comparing (A18) and (A19) with (A15) (A16) we obtain the expression for the effective stiffness and damping factors as follows:

$$(A20) \quad K_x' = M_e + \mathcal{R} \left\{ \frac{ps - rq}{us - vq} \right\}$$

$$(A21) \quad K_y' = M_e + \mathcal{R} \left\{ \frac{-i(ps - rq)}{vp - ur} \right\}$$

$$(A22) \quad C_x' = \mathcal{I} \left\{ \frac{ps - rq}{us - vq} \right\}$$

$$(A23) \quad C_y' = \mathcal{I} \left\{ \frac{-i(ps - rq)}{vp - ur} \right\}$$

The correlation between the experimental and theoretical characteristics of the test bearing can be achieved by comparing the theoretical and experimental effective stiffness and damping factors. The experimental effective stiffness and damping factors are calculated from motions measured at A and O' using Equations (A18) and (A19) while the theoretical  $K_x'$ ,  $K_y'$ ,  $C_x'$  and  $C_y'$  are determined by Equations (A20) through (A23).

# REFERENCES

1. Reichardt, H. ZAMM 31, 208 (1961)
2. Elrod, H.G. J.Aero. Science, 24, 460 (1957)
3. Hagg, A.C. and Sankey, G.O., "Some Dynamic Properties of Oil Film Journal Bearings with Reference to Unbalance Vibration of Rotors", J. Appl. Mech. 302-306, June, 1956.
4. Smith, M.I. and Fuller, D.D., "Journal Bearings Operating at Super Laminar Speeds," A.S.M.E. Vol. 78, 1956.
5. Arwas, E.B., Orcutt, F. K., and Vohr, J.H., "Lubrication Analysis in Turbulent Regime, 1st Quarterly Report," M.T.I. Report 63TR47, 1963. Work performed under NASA Contract NAS w-771.
6. Ng, C.W., "Fluid Dynamic Foundation of Turbulent Lubrication Theory," M.T.I. Report 63TR27, 1963. Work performed under A.I. Subcontract N2S9-1599.
7. Pan, C.H.T. and Ng, C.W., "A Linearized Turbulent Lubrication Thrust," M.T.I. Report 63TR53, work performed under A.I. Subcontract N2S9-1599.
8. Knudsen, J.G. and Katz, D.L. "Fluid Dynamics and Heat Transfer," McGraw Hill Book Co. 1958, Section 7-5. See also: Hinze, J.O., "Turbulence," McGraw Hill Book Co. 1959, Section 7-5.
9. Orcutt, F.K., "Investigation of a Partial Arc Pad Bearing in the Super Laminar Flow Regime," To be presented at ASME Lubrication Symposium, Cleveland, Ohio, April, 1964.
10. Taylor, G.I., "Stability of a Viscous Liquid Contained Between Two Rotating Cylinders," Phil. Trans., v. 223, 1923, pp 289-343.
11. Cole, J. A., "Experiments on the Flow in Rotating Annular Clearances," paper presented at the Conference on Lubrication and Wear, Institution of Mechanical Engineers, London, Oct. 1957.
12. DiPrima, R.C., "A Note on the Stability of Flow in Non-Concentric Annuli," M.T.I. Technical Report MTI 62TR15 Aug. 1962.
13. Walowit, J., Tsao, S., and DiPrima, R.C., "Stability of Flow Between Arbitrarily Spaced Concentric Cylindrical Surfaces Including The Effect of a Radial Temperature Gradient," Rensselaer Polytechnic Institute, RPI Math. Rep. No. 61, Aug. 1963.
14. Townsend, A.A., "The Development of Turbulent Boundary Layers with Negligible Wall Stress," Journal of Fluid Mechanics, Vol. 6 1960, pp. 143-155.

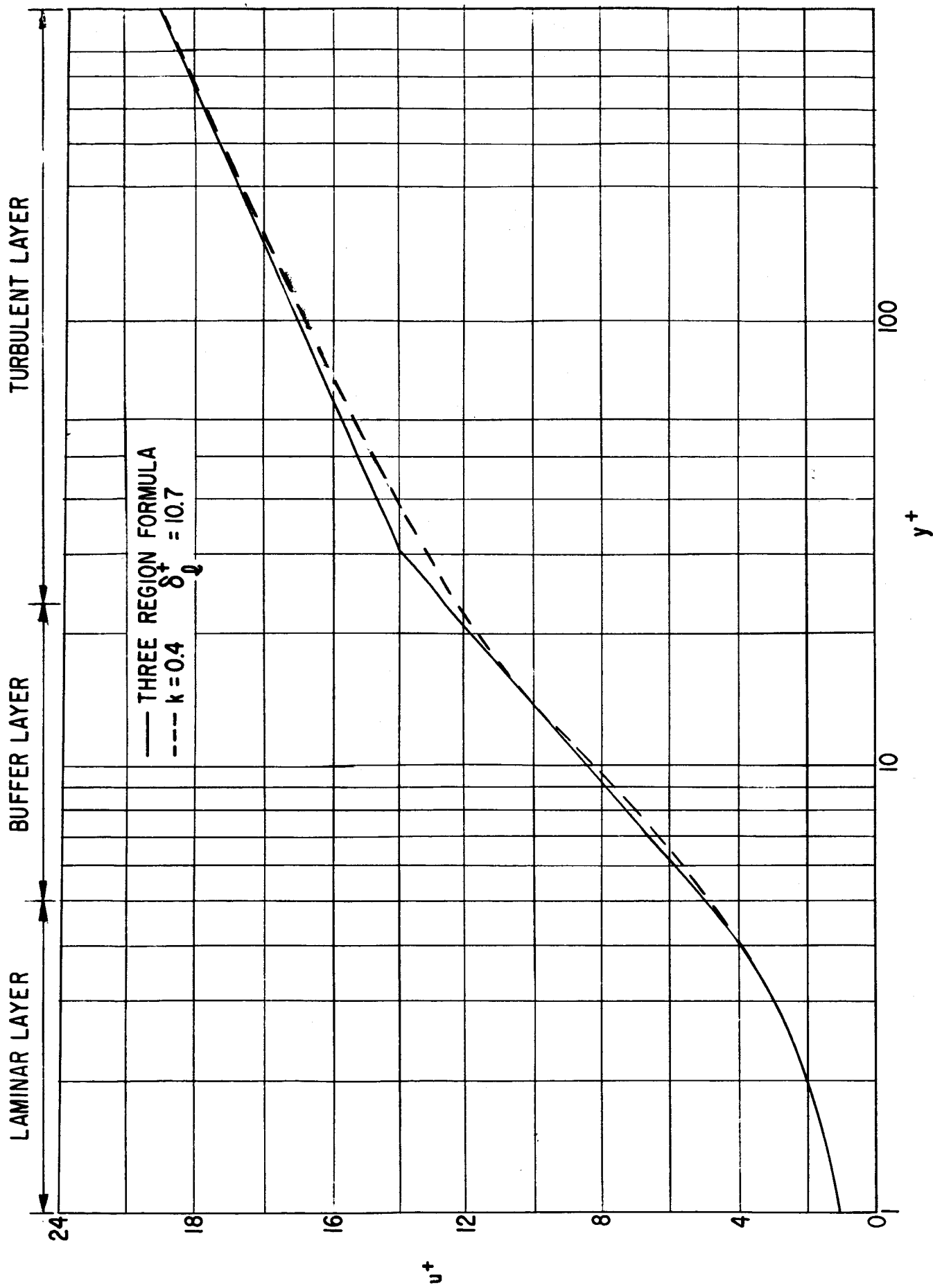


Fig. 1 Universal Velocity Distribution Plot



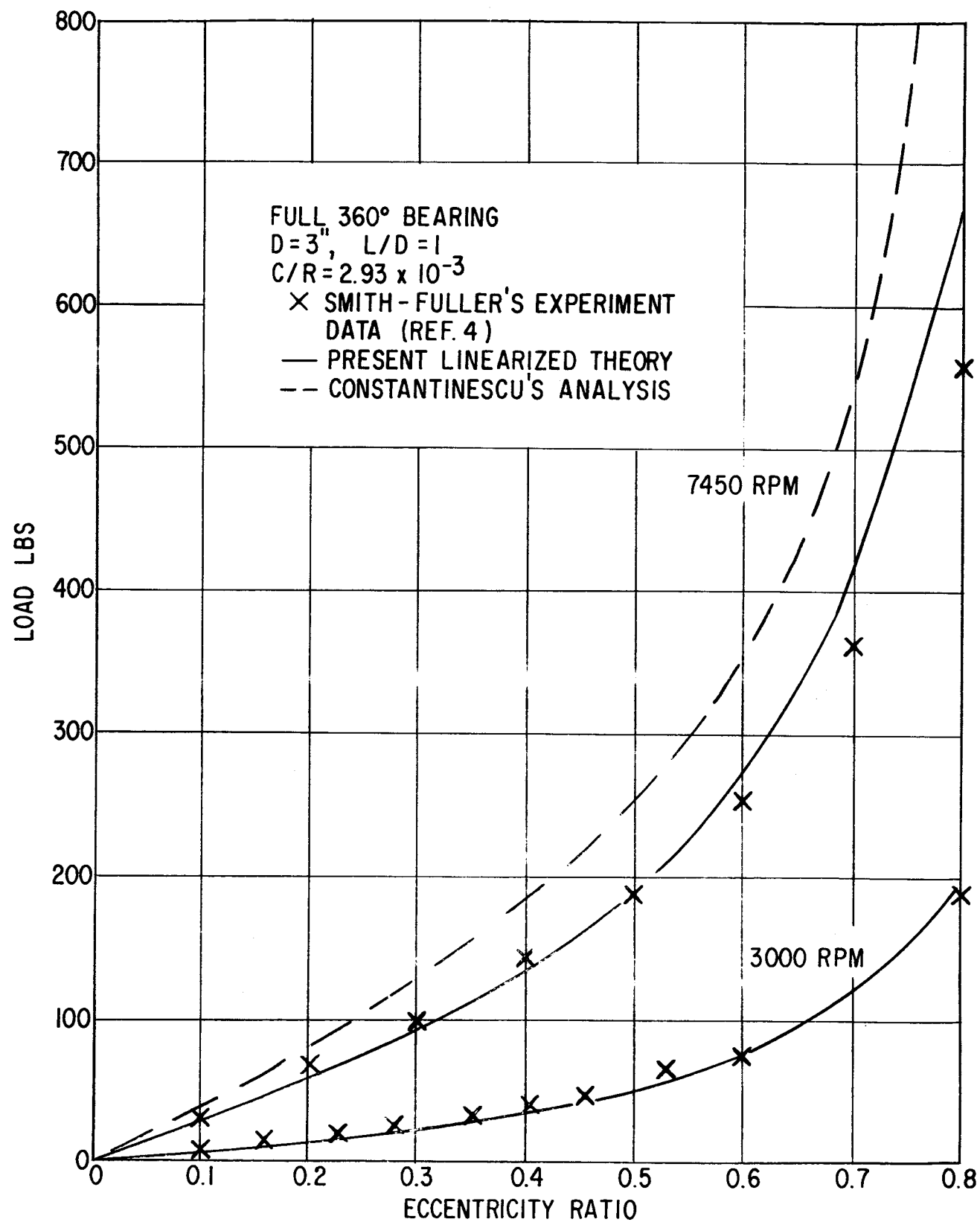


Fig. 2a Load vs Eccentricity Ratio

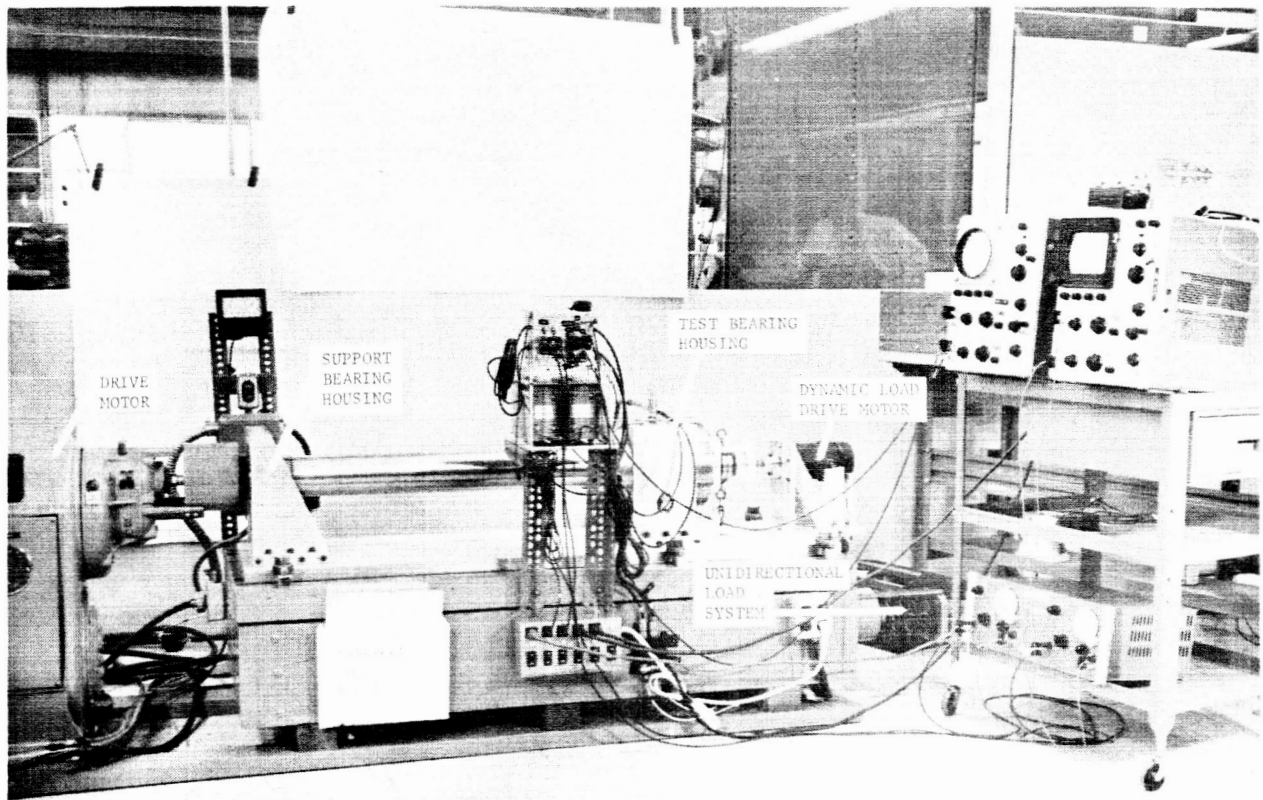


Fig. 3 Dynamic Load Bearing Apparatus

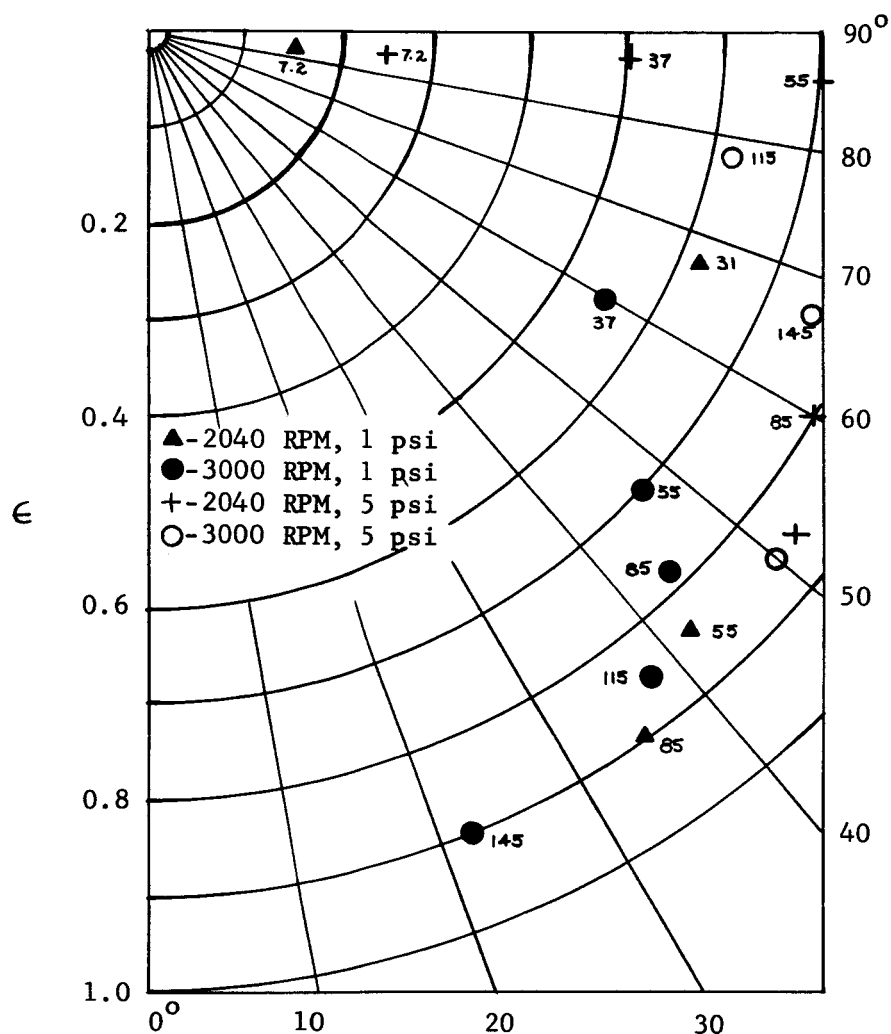


Fig. 4 Shaft Locus Measurements At Several Oil Feed Pressures With 360 Degree Bearing

$C/R = 4 \times 10^{-3}$ ,  $L/D = 1.0$ , 4 inch Diameter  
 Feed from 1/4 inch Diameter Hole  
 180° from load line  
 Numerals are load in pounds

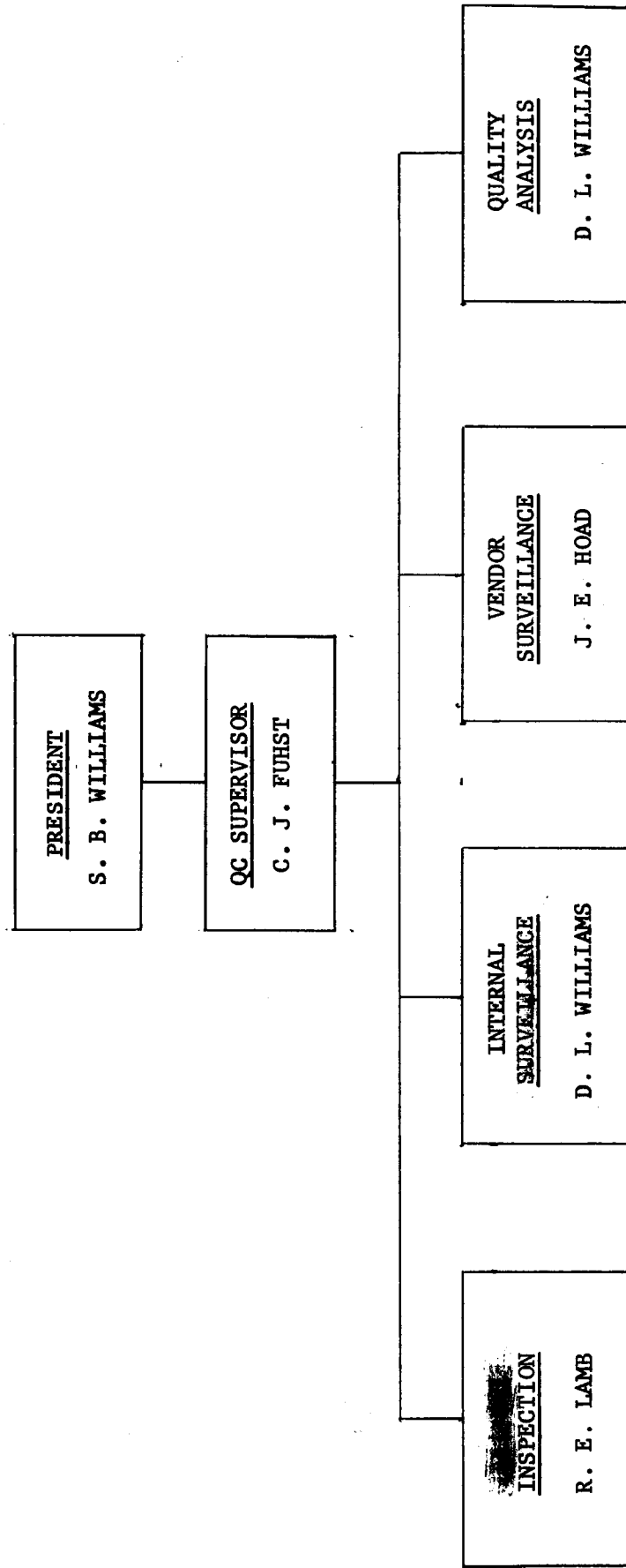
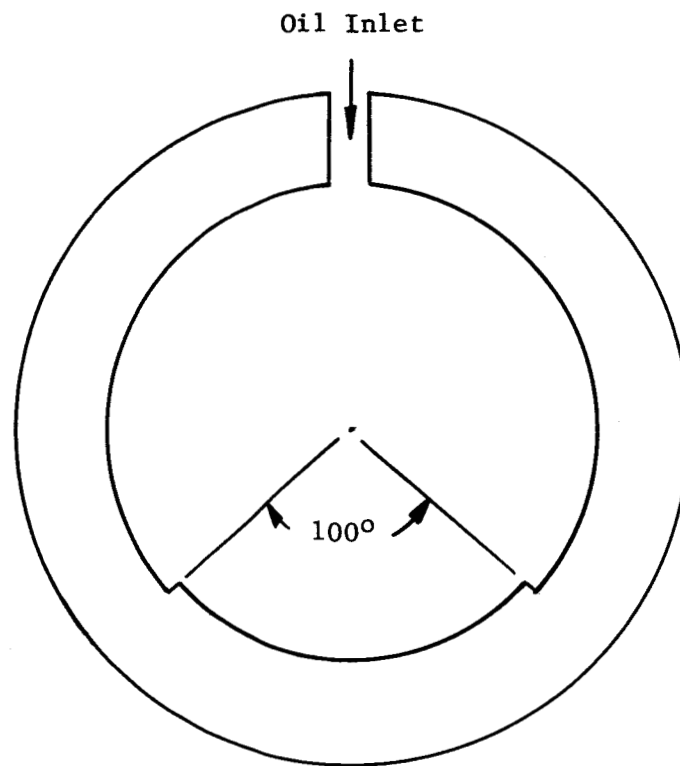
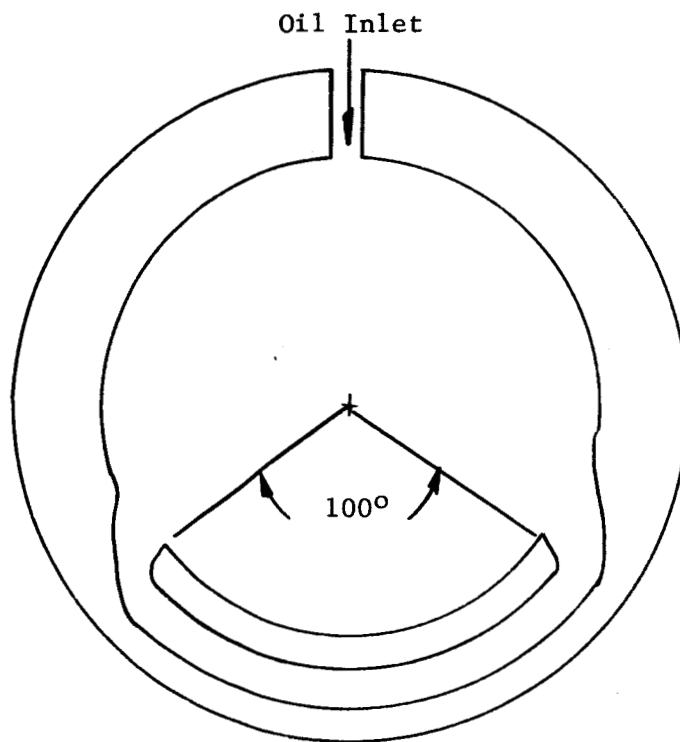


FIG. 5

WILLIAMS RESEARCH CORPORATION QUALITY ASSURANCE ORGANIZATION



(a) Plain



(b) With Bypass Grooves

Fig. 5 Schematic View of Partial Arc Bearing Designs

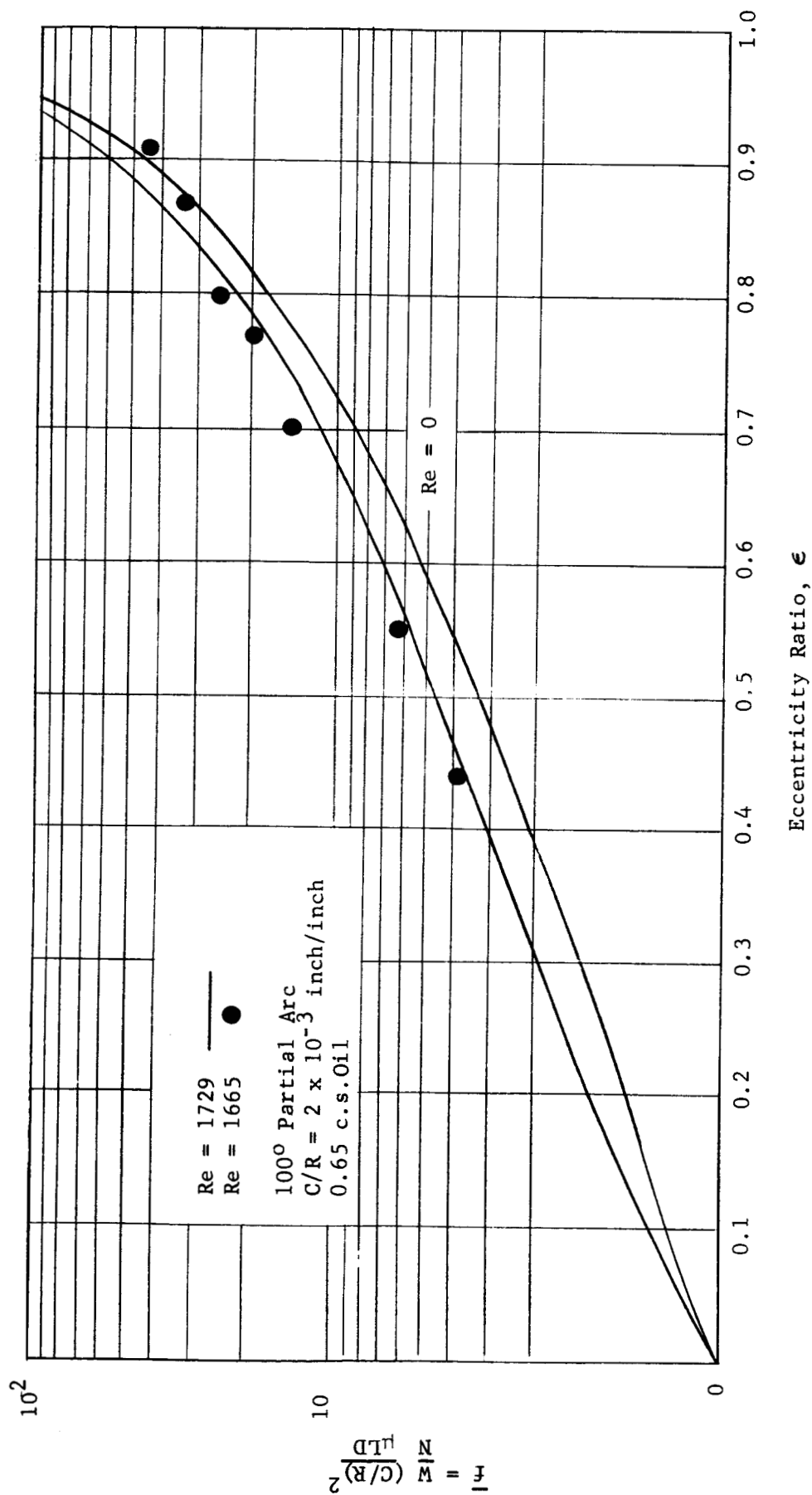


Fig. 6 Steady State Load Capacity - Reynolds Number 1665

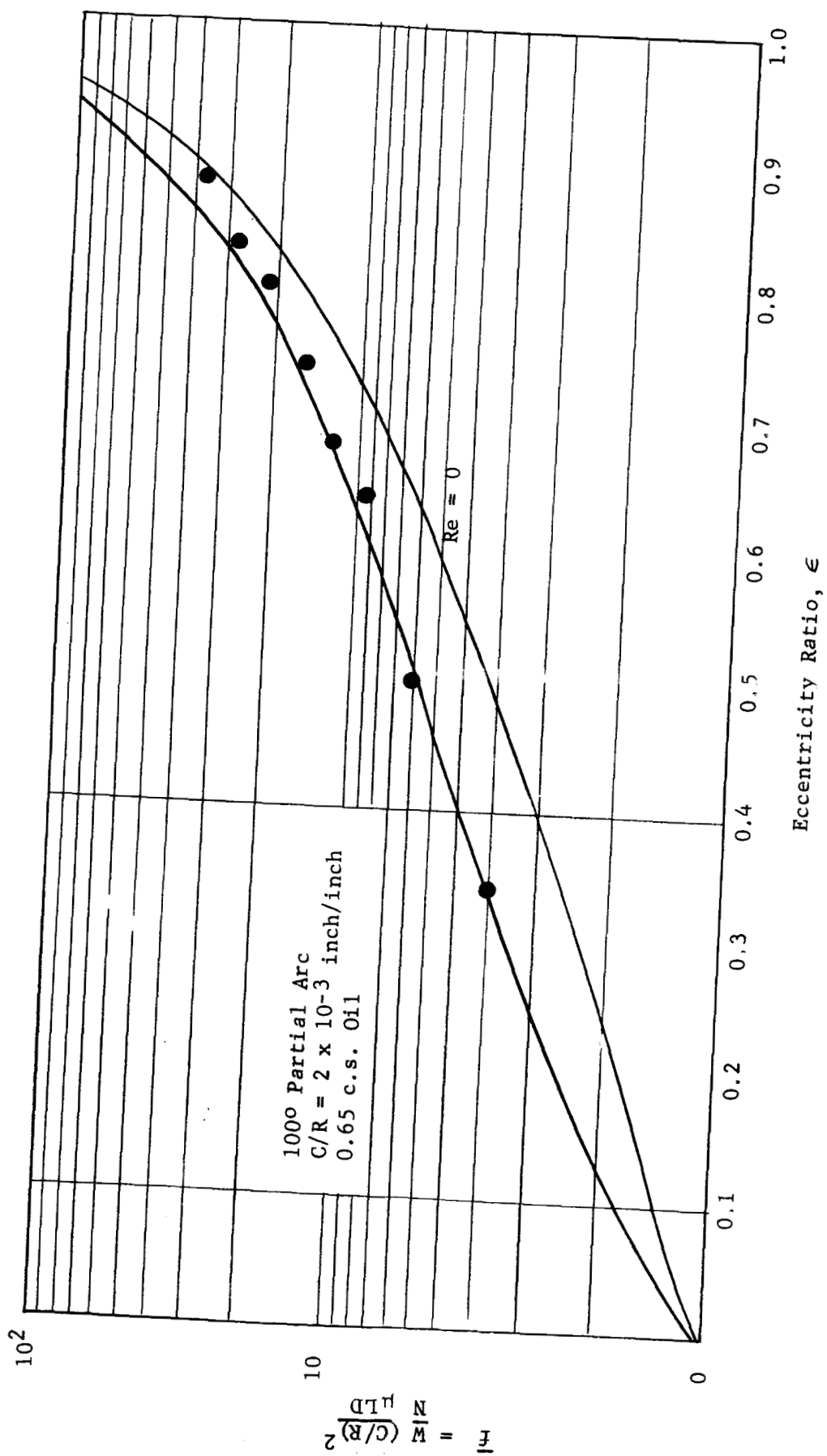


Fig. 7 Steady State Load Capacity - Reynolds Number 3326

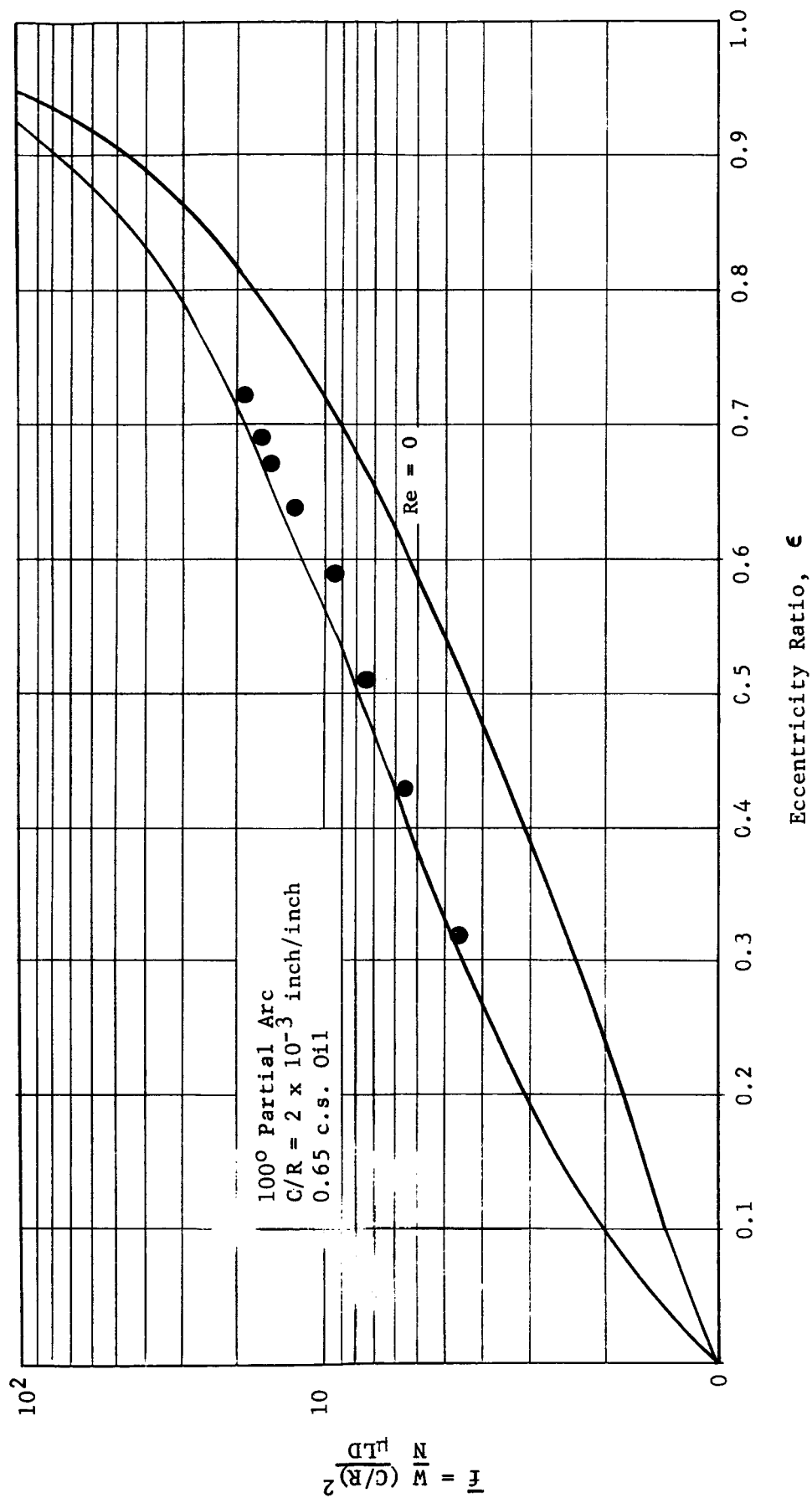


Fig. 8 Steady State Load Capacity - Reynolds Number 5820



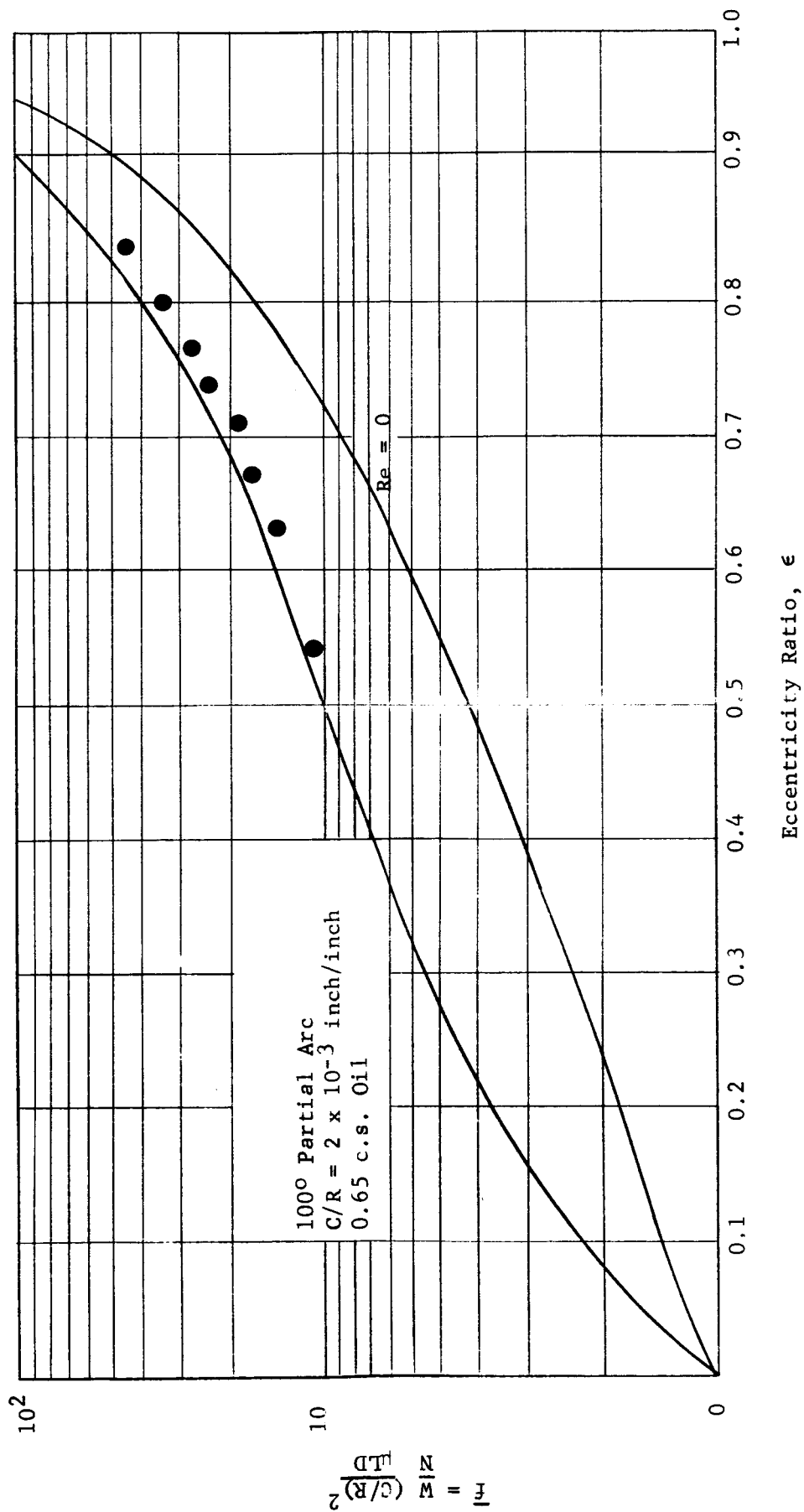


Fig. 9 Steady State Load Capacity - Reynolds Number 8314

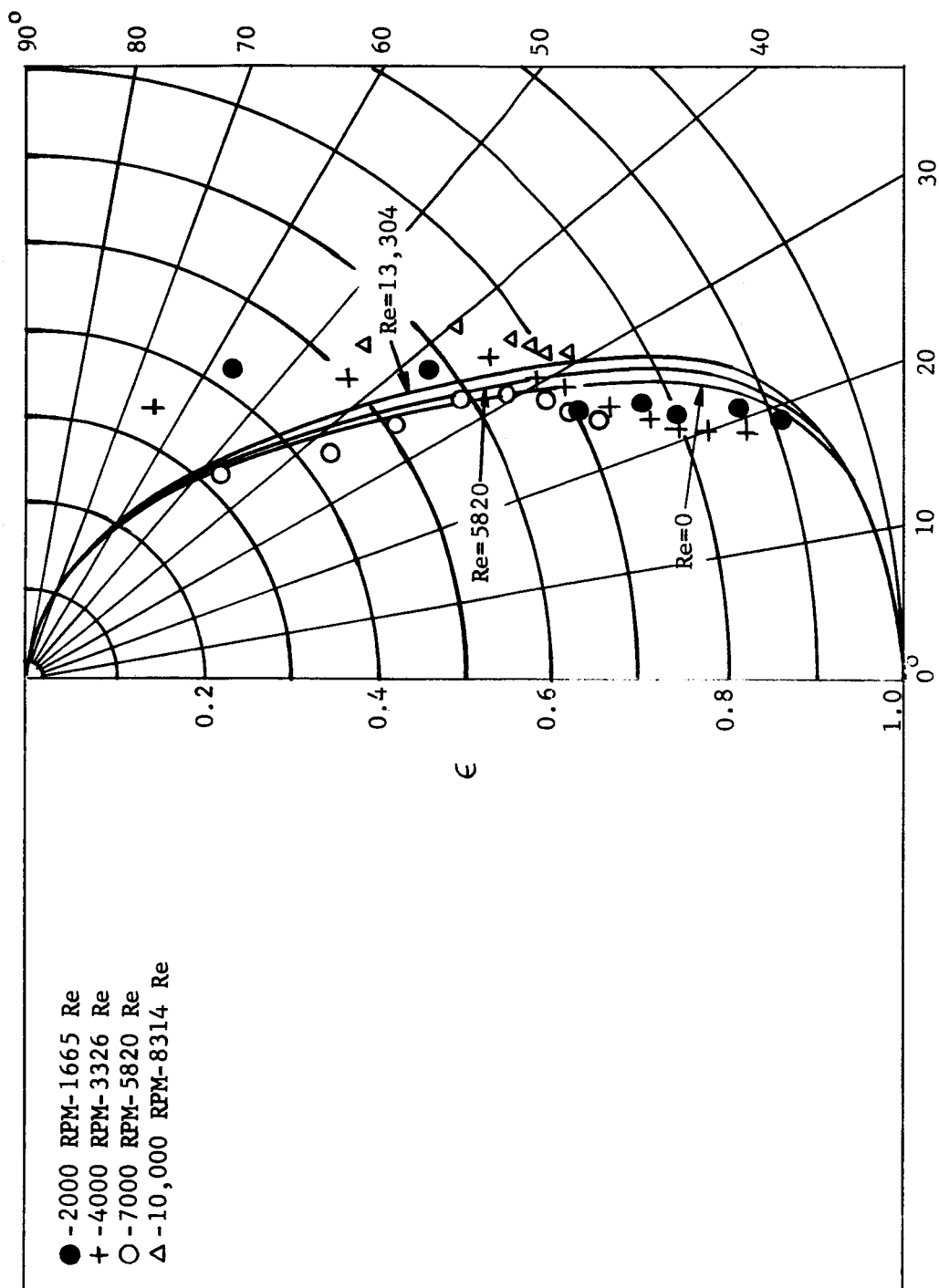


Fig. 10 Eccentricity - Attitude Angle Measurements

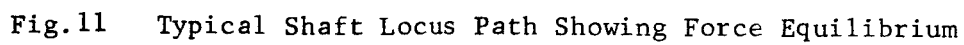


Fig.11 Typical Shaft Locus Path Showing Force Equilibrium

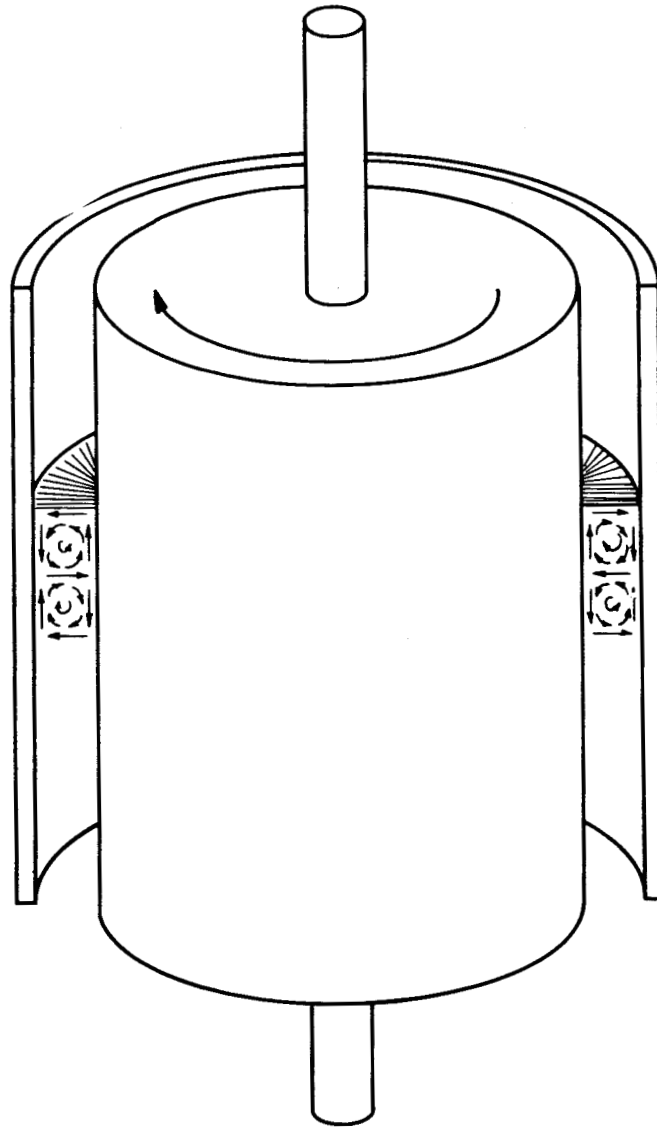


FIG.12 VELOCITY PATTERN IN TAYLOR VORTEX PAIR

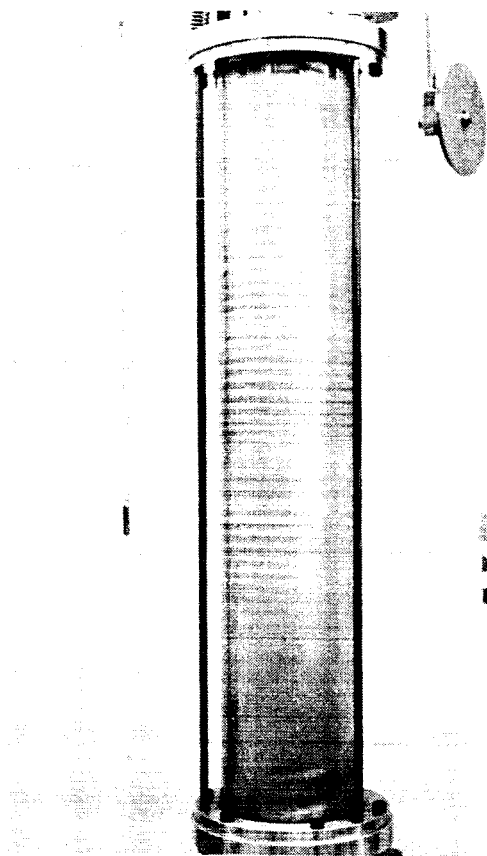


Fig. 13 Test Section With Taylor  
Vortices Just Beginning To  
Develop.

Rotational Speed = 2.69 RPS

$$\sqrt{1/2T_a} = 53$$

$$\epsilon = 0.475$$

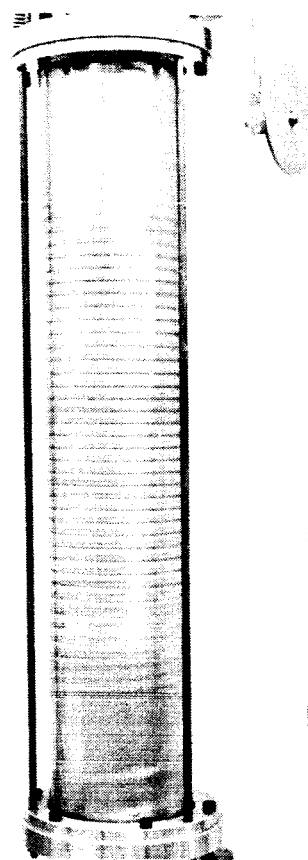


Fig. 14 Test Section Just At Point  
Where Taylor Vortices Are  
Developed.

Rotational Speed = 2.99 RPS

$$\sqrt{1/2T_a} = 59.4$$

$$\epsilon = 0.475$$

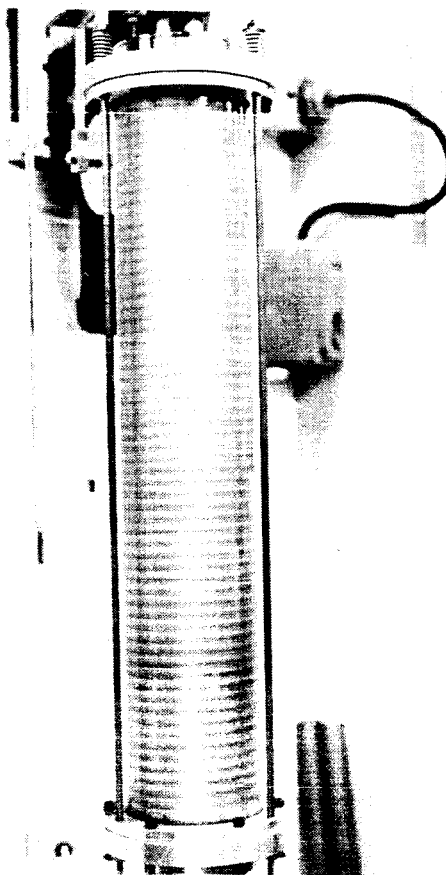


Fig. 15 Fully Developed Taylor Vortices  
for Concentric Cylinders.

Rotational Speed = 2.26 RPS

$$\sqrt{1/2T_a} = 42.6$$

$$\epsilon = 0$$

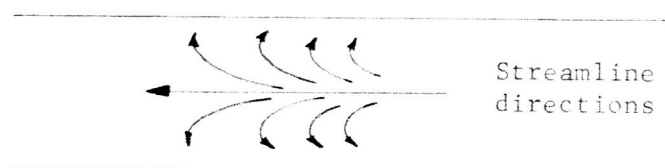
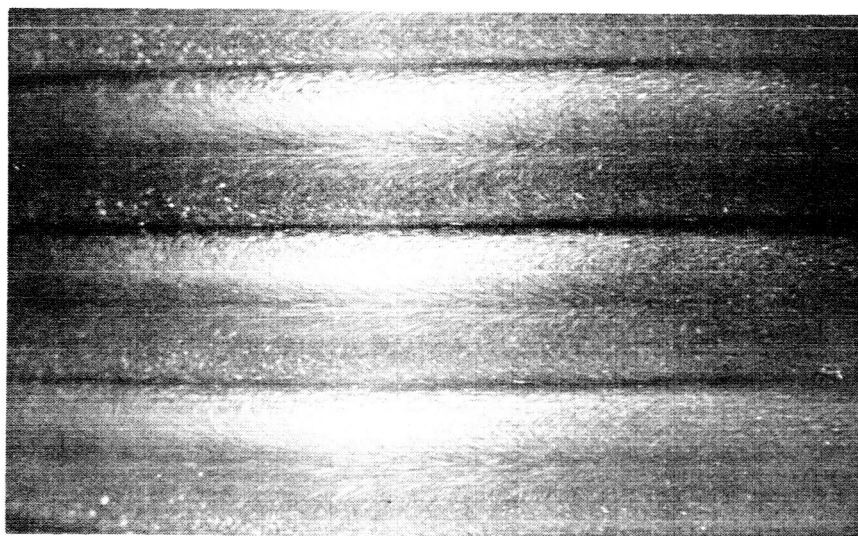


Fig. 16 Closeup of Vortex Flow With  
Diagram Indicating Directions  
of Streamlines.

$$\epsilon = 0.475$$

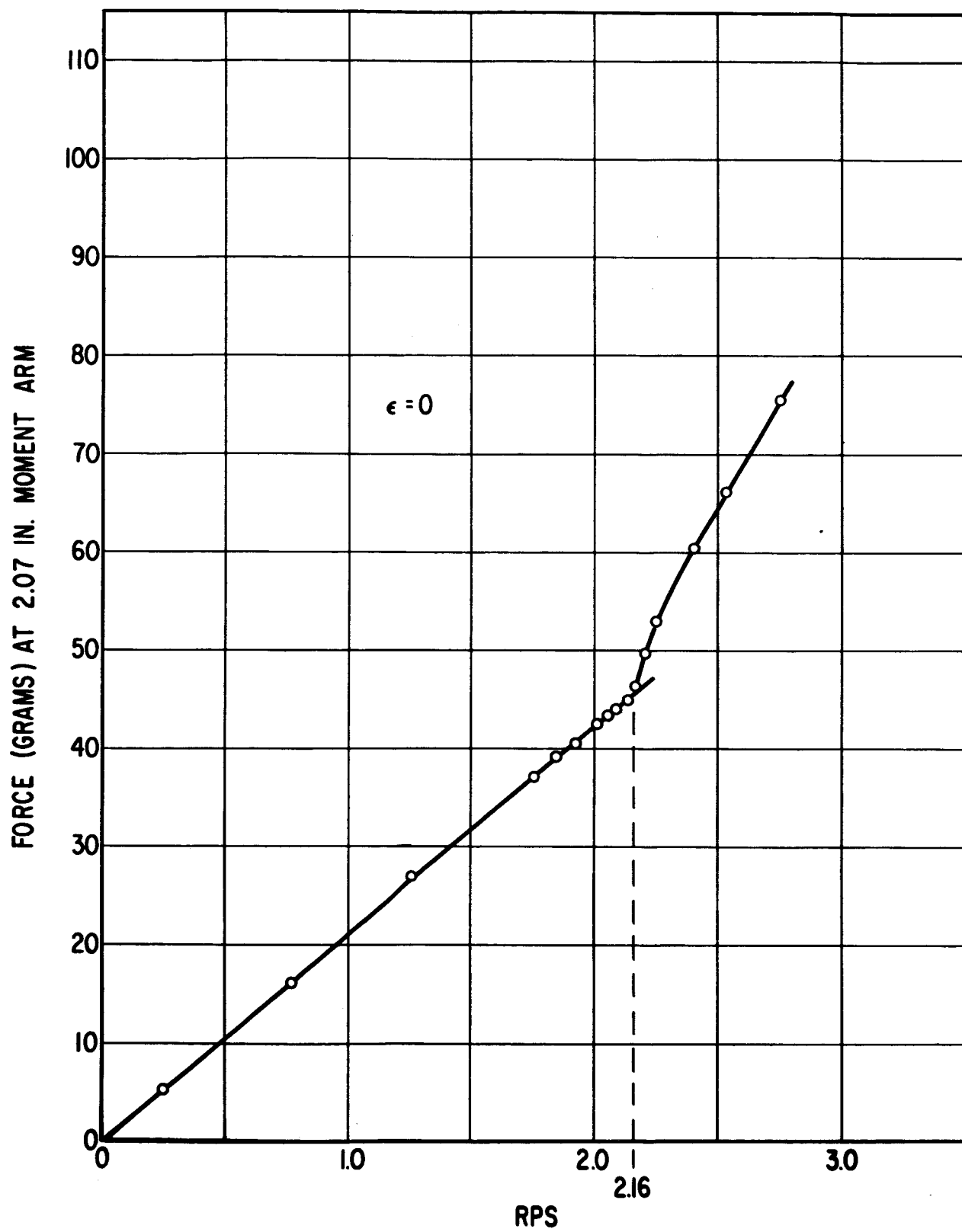


FIG.18 TORQUE vs SPEED



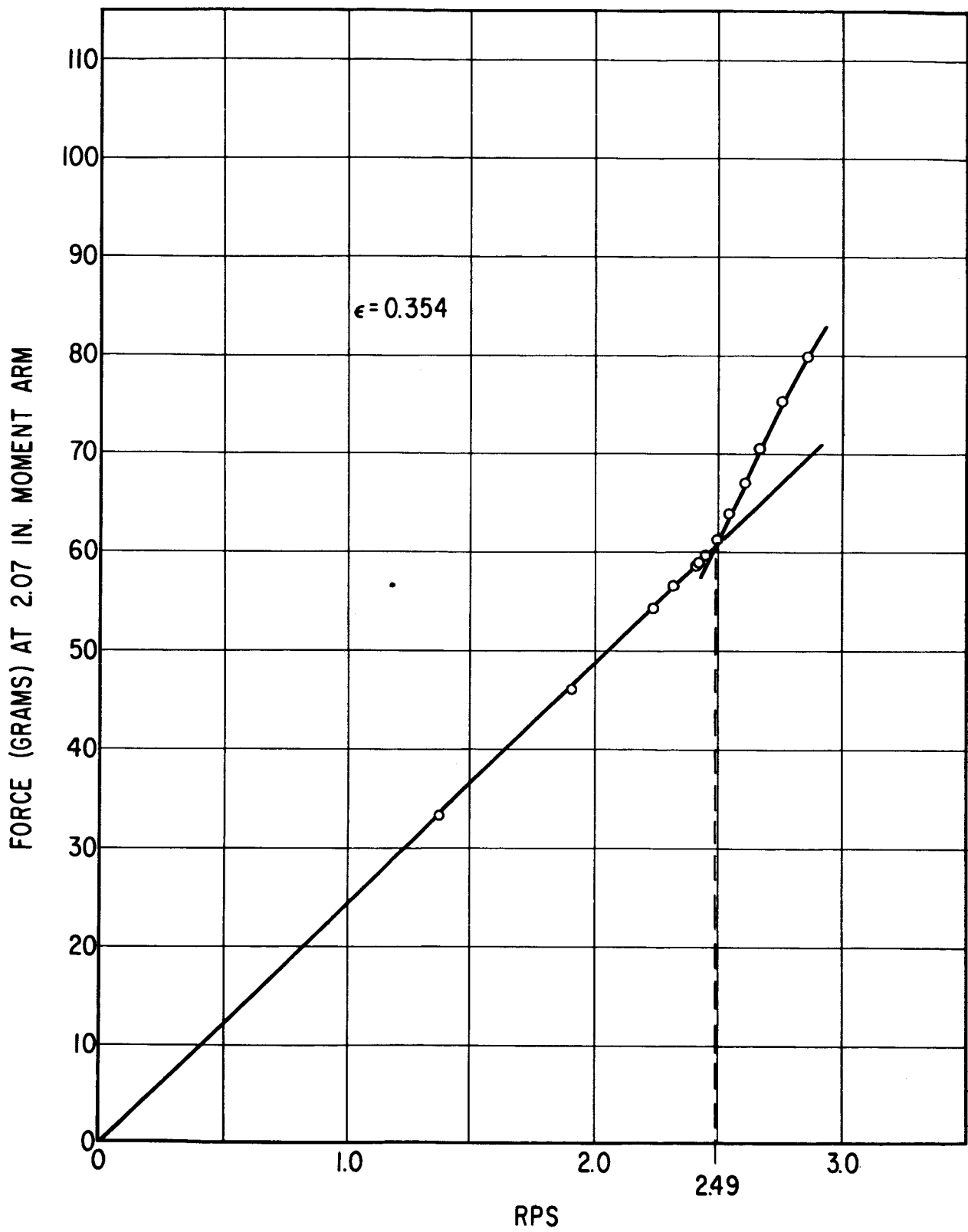


FIG.19 TORQUE vs SPEED

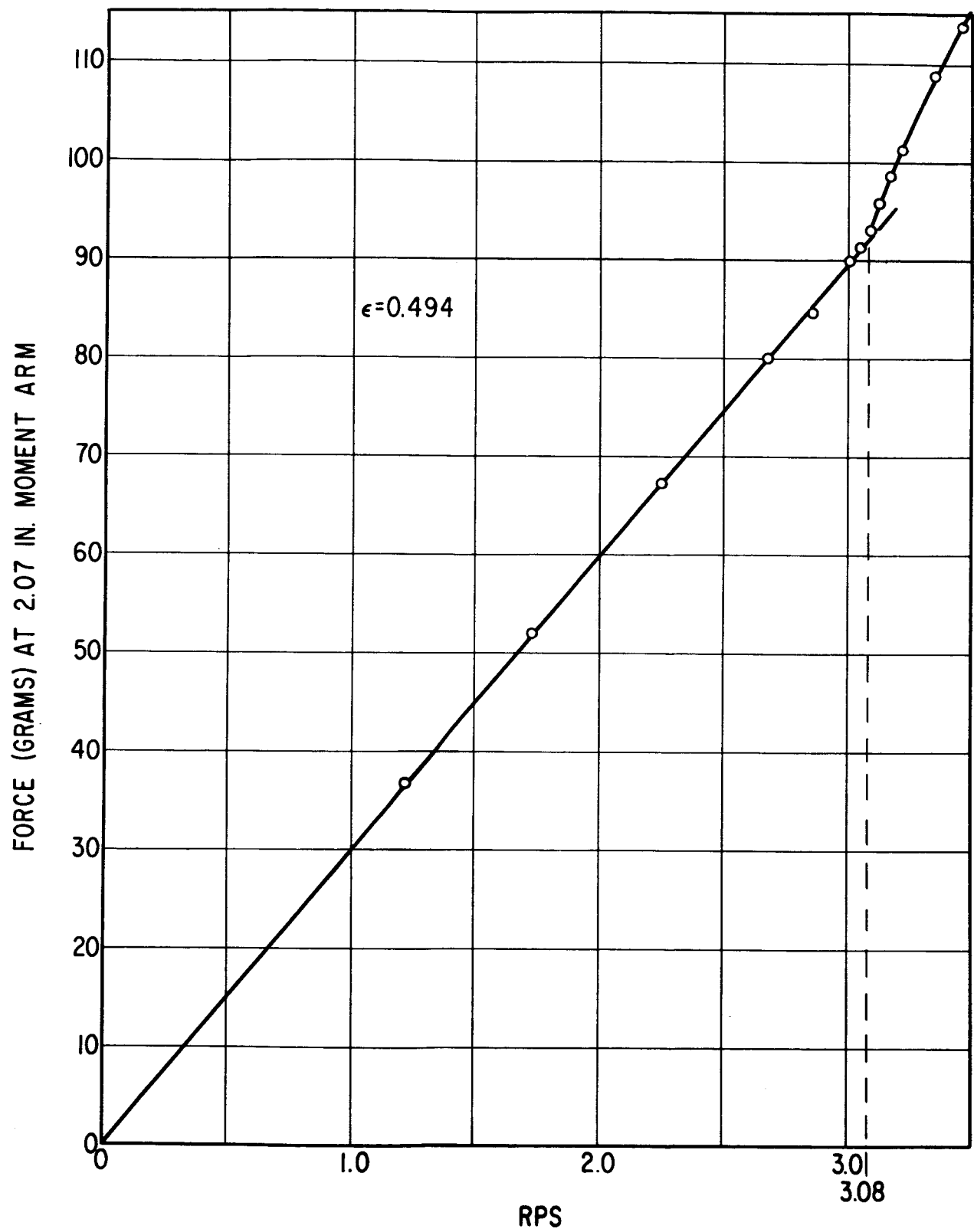


FIG. 20 TORQUE vs SPEED

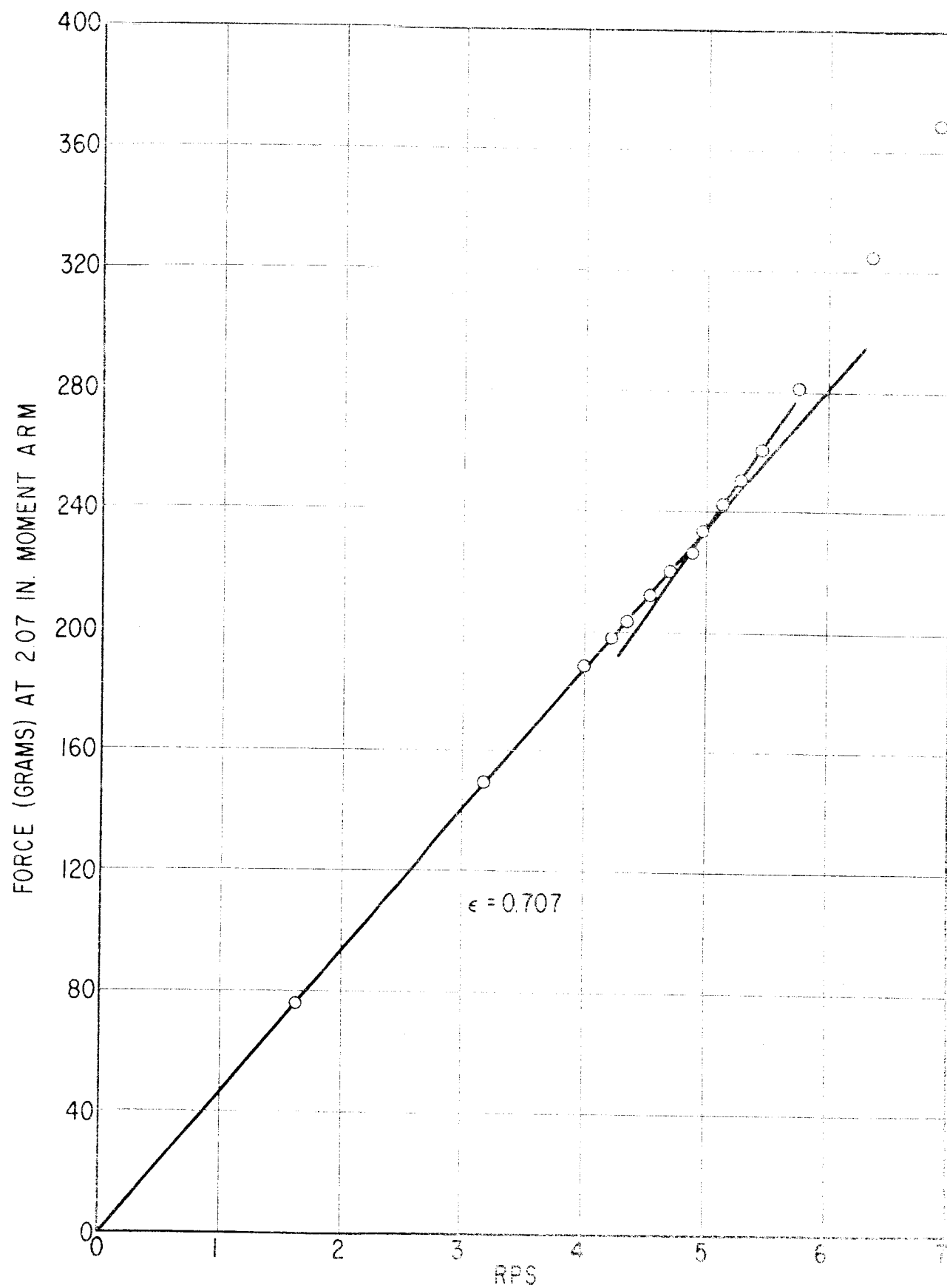


FIG. 21 TORQUE vs SPEED

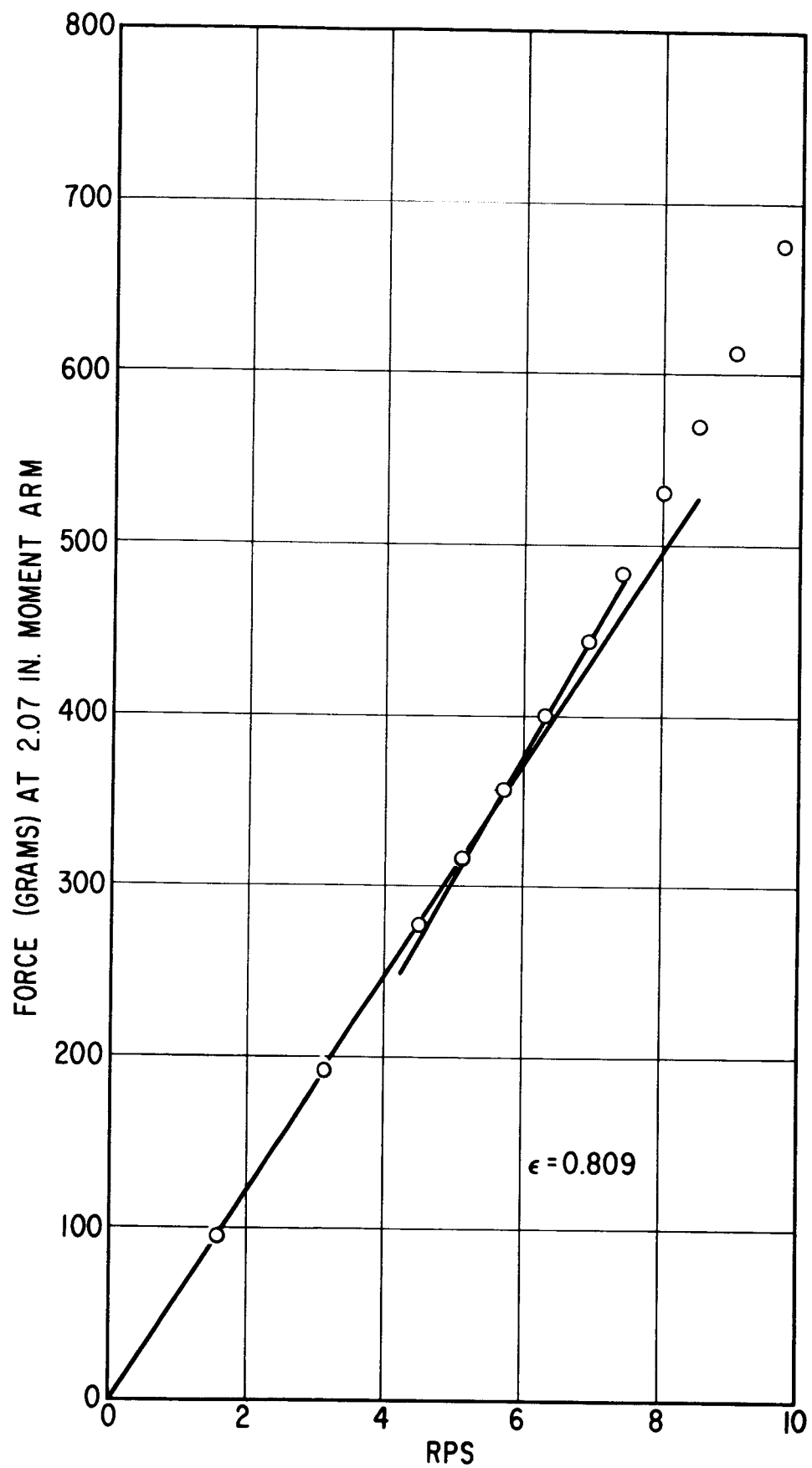


FIG. 22 TORQUE vs SPEED

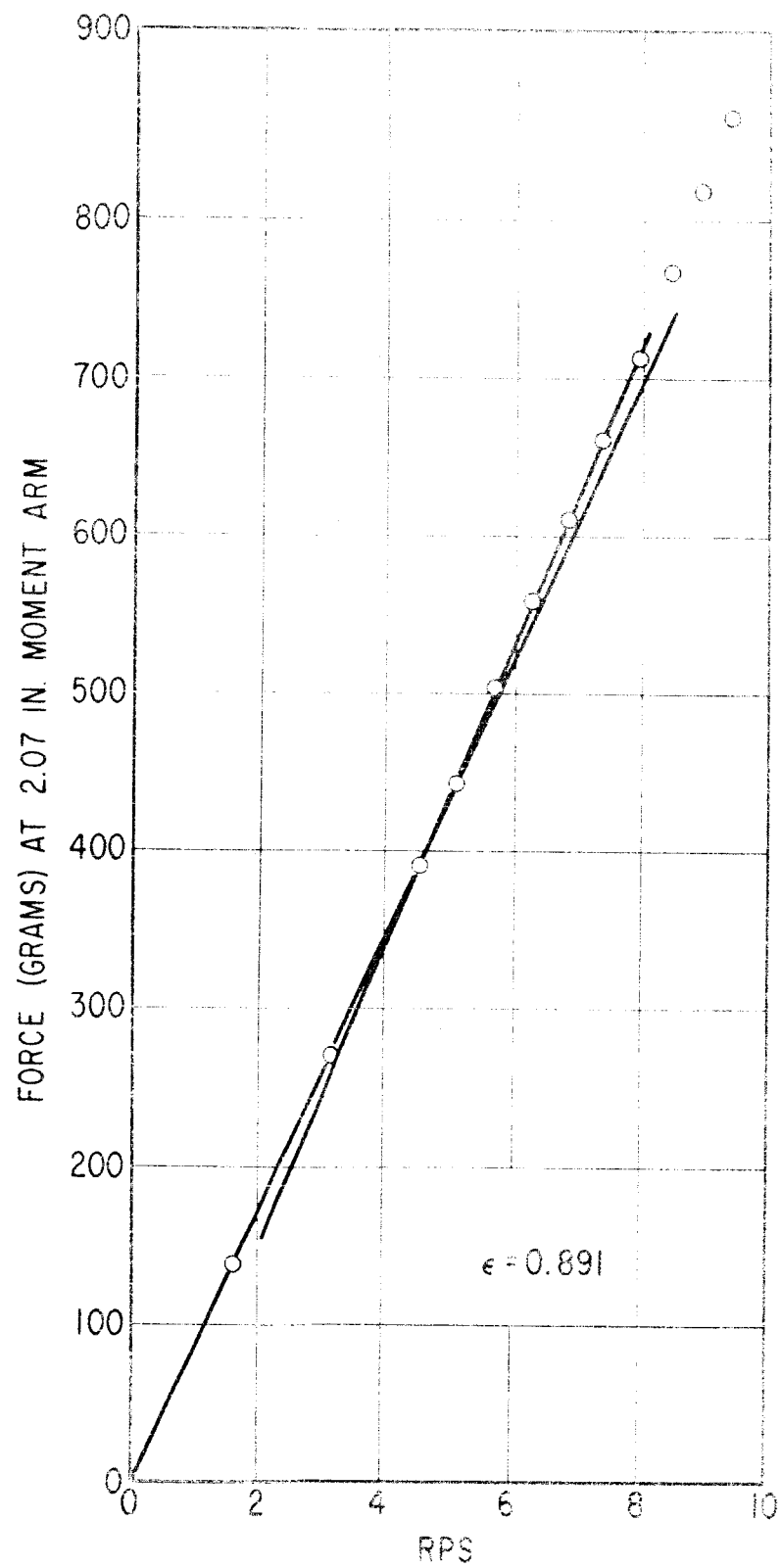


FIG. 23 TORQUE vs SPEED

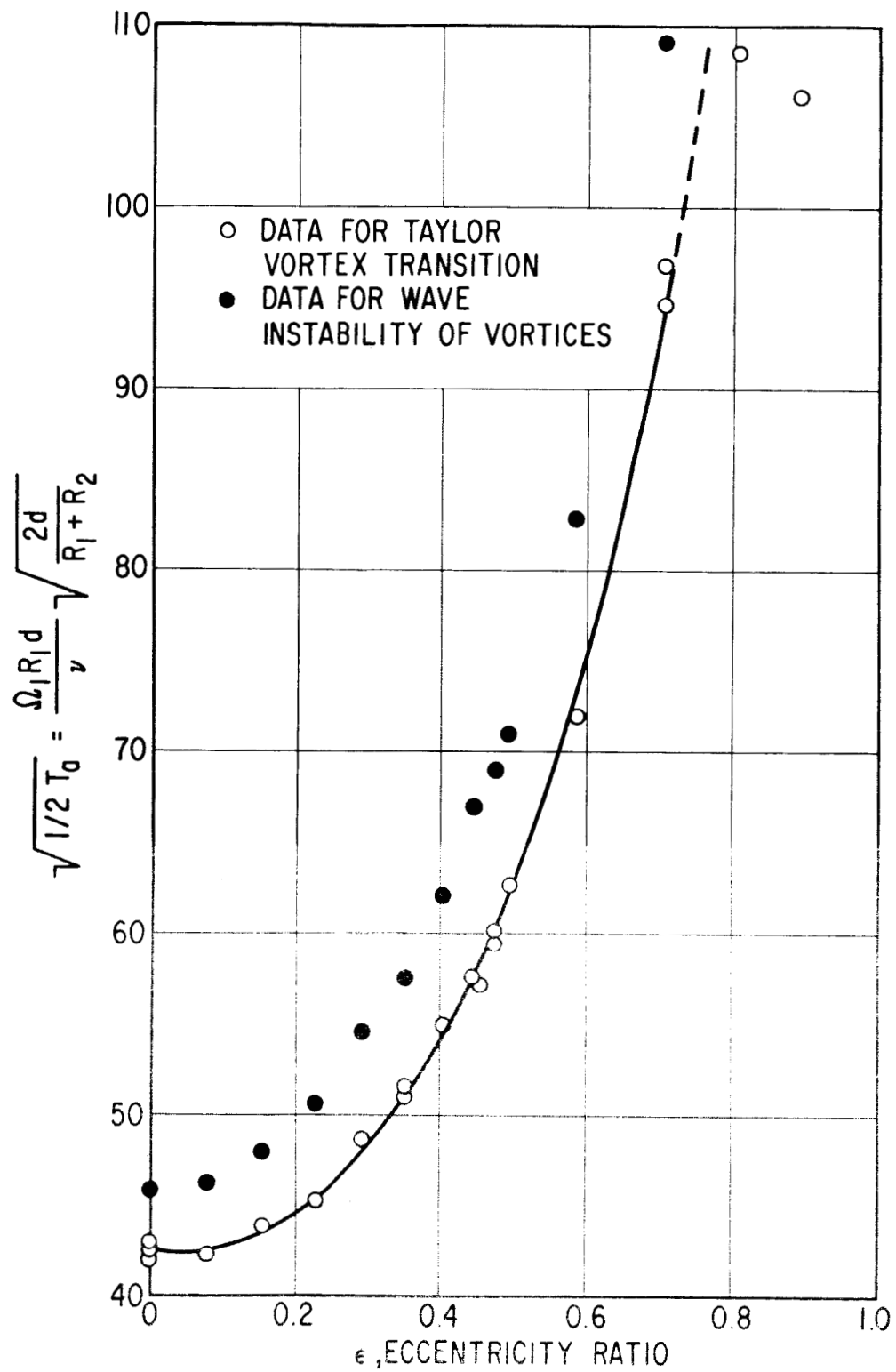


FIG.24 CRITICAL SPEED DATA FOR NON-CONCENTRIC CYLINDERS

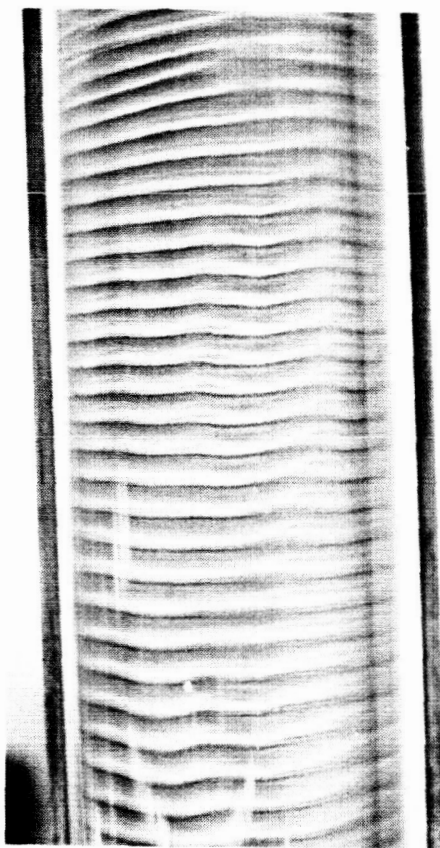


Fig. 25    Photograph showing Vortex Wave  
Instability for Non-Concentric  
Cylinder.

$$\epsilon = 0.475$$

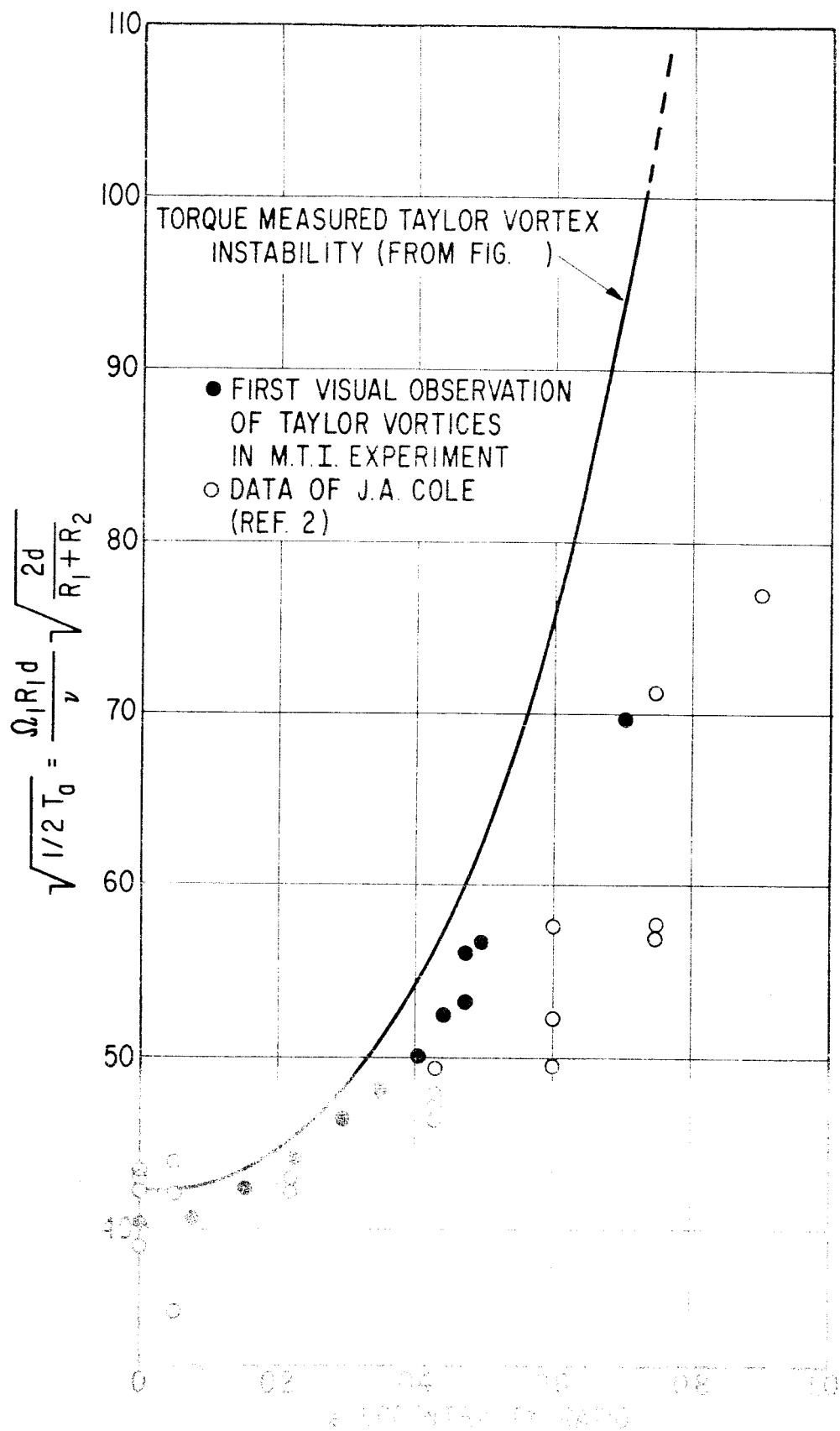


FIG.26 COMPARISON OF M.T.I. DATA WITH THOSE OF J.A. COLE



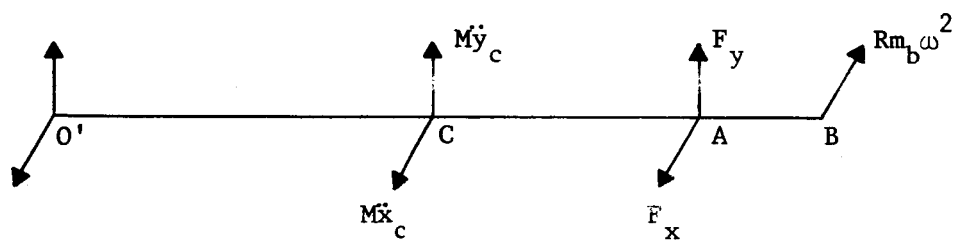


Fig. 27 Forces Acting On Experimental Rotor